Part 2: Leader decay and reactivation

Les Renardières Group

Indexing terms: *Arcing, Breakdown and gas discharges, Gas discharges, Load and voltage regulation, Insulators and insulation, Overvoltages*

Abstract: The behaviour of large air-insulated structures subjected to complex multiple-peak surge overvoltages is influenced by the presence of already established leader overvoltages in influenced by the presence of already established leader development in the space. The decay processes of a positive leader channel following current interruption appear not to have been studied in detail, and Part 2 provides electrical and optical measurements of leader decay and reactivation in a 6 m rod-plane gap. It is found that, for a positive leader created by a switching impulse (SI) of critical time to crest, the leader path could be rapidly reactivated over at least part of its length by a second voltage application at times of up to about 1 ms after its original formation. For longer times, new leader growth may still retrace the original basic leader path. The temporal and spatial characteristics of the reactivated leader are substantially different from those of the basic leader. The causes of the large statistical variation in behaviour are discussed. The results presented should provide the basis for improved physical knowledge of the leader and corona processes, and contribute to improved engineering models for insulation co-ordination.

1 Introduction

The aim of this investigation is to study how a leader channel, which has already been created in an airgap but which in the case of a voltage withstand has naturally ended its propagation, will behave when subsequent overvoltages are applied. The experiment was performed using a rod-plane gap with a horizontal axis (see Part 1). To produce the necessary overvoltage sequence, the rod and the plane were successively energized, respectively, with a positive and a negative impulse. This represented the most practicable available way of simulating double-peak surges (surge type A, Part 1). Fig. 1 gives the definition of the voltage parameters used.

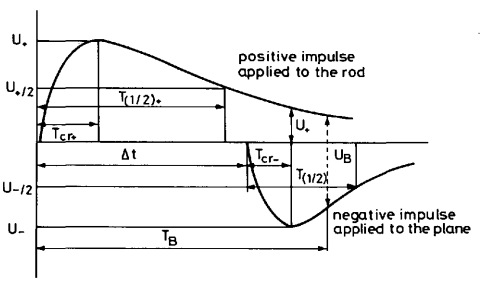

Fig. 1 *Definition of the voltage parameters*

The time to crest of the positive impulse T_{cr+} was 240 μs. This value corresponds to the standards and is also around the critical time to crest value for a 6 m gap. Two different tail shapes were used: $T_{(1/2)+} = 1650$ μs and 9000 μs. The crest level of the positive impulse U_+ was kept constant during the whole experiment at 1390 kV. This value is a compromise between a too low level which would allow only for short positive leaders to be created, and a too high level which would result in a high breakdown probability during the positive impulse. After various time delays Δt, in the range from 400 to 2000 μs, the negative impulse was applied to the plane. Two different time to crest values T_{cr-} (2 μs and 40 μs) and two times to half value (30 μs and 150 μs) were used. The crest level of the negative impulse U_- was varied in the range from 500 to 1200 kV.

In the following Sections, the breakdown characteristics are given, which show the reduction in electrical strength of the test gap which is caused by a pre-existing leader. The important recovery of the electrical strength is thus due to the decay of the leader. The phenomenological structure and sequence of the reactivation process is then described, as the underlying cause of the change in the macroscopic parameters.

The detailed nature of the leader reactivation is shown to be dependent on (i) the controllable parameters, which are the delay between the original leader formation and the second voltage increase, the shape of this increase and its amplitude, and (ii) the uncontrollable parameters determined by the characteristics of the original leader channel. The work forms a contribution to the practical objective of modelling the behaviour of air insulation which is subjected to multiple-peak surges.

2 Breakdown characteristics

2.1 Effect of time delay

Table 1 gives the different combinations between the positive and the negative impulses which were tested, as well as

Table 1: Characteristics of the tested combinations

Combinations	$T_{cr+}/T_{(1/2)+}$ μs	$T_{cr-}/T_{(1/2)-}$ μs	Number of shots	Number of breakdowns	$T_{B\,min}$ μs	$T_{B\,max}$ μs
1(a)–1(f)	240/9000	40/165	147	16	164	228
2(a)–2(f)	240/1650	40/165	65	10	210	257
3(a)–3(f)	240/9000	2.5/30	60	4	215	256
4(a)–4(f)	240/9000	2/150	56	3	212	256

Paper 4826A (S3), received 14th January 1986

For the author details see Paper 4825A, Double-impulse tests of long airgaps Part 1

the total number of shots applied for each combination. In some cases (about 10% of the shots), breakdown occurs on the positive impulse. The number of such events is given together with the minimum and maximum time to breakdown in the last columns of Table 1.

Tables 2 to 5 give, for each series, the different situations (Δt, U_-) which were tested, the positive component u^+ applied to the rod at time $\Delta t + T_{cr-}$, the number of shots (excluding those for which breakdown occurred on the positive impulse), the number of breakdowns, the range of the time to breakdown values, and the average voltage at breakdown.

From Tables 2 and 3, it can be seen that the breakdown probability increases with U_- and an estimation of the 50% breakdown voltage can be obtained. The variation of this breakdown voltage is plotted in Fig. 2, together with the amplitude of the positive voltage component applied to the rod as a function of the time delay Δt. It can be seen that $U_{-50\%}$ increases with Δt. This increase of the negative voltage is accounted by two factors.

The first and obvious factor is the compensation for the decrease of the positive voltage applied to the rod. Unfortunately, this effect cannot easily be quantified. As shown by field computation (see Part 1), the relative contribution

Table 2: Combination 1 breakdown parameters

Combination	Δt μs	u_+ kV	U^- kV	Number of shots	Number of breakdowns	$(T_B - \Delta t)_{min}$ μs	$(T_B - \Delta t)_{max}$ μs	U_B kV
1(*a*)	400	1382	505	7	0	—	—	—
			595	11	5	37	107	1977
			695	10	6	38	88	2077
1(*b*)	800	1340	690	6	0	—	—	—
			795	4	1	48	48	2135
			895	15	10	37	106	2235
			990	10	10	36	68	2335
1(*c*)	1000	1315	690	10	0	—	—	—
			795	9	5	61	93	2120
			890	8	6	38	76	2205
			990	6	3	54	72	2305
1(*d*)	1150	1295	990	13	10	52	116	2285
1(*e*)	1300	1280	990	9	2	70	79	2270
			1095	7	5	43	143	2375
1(*f*)	1800	1225	1200	6	1	47	47	2425
				131				

u_+ = instantaneous value at time Δt of positive impulse (crest voltage 1390 kV)

Table 3: Combination 2 breakdown parameters

Combination	Δt μs	u_+ kV	U^- kV	Number of shots	Number of breakdowns	$(T_B - \Delta t)_{min}$ μs	$(T_B - \Delta t)_{max}$ μs	U_B kV
2(*a*)	400	1305	790	8	2	57	58	2095
			840	8	3	26	96	2140
			895	7	6	41	101	2200
2(*b*)	500	1250	890	8	0	—	—	—
			980	7	5	31	77	2230
2(*c*)	600	1190	1090	6	0	—	—	—
			1205	6	5	26	65	2390
2(*d*)	800	1080	1200	5	2	50	52	2280
				55				

u_+ = instantaneous value at time Δt of positive impulse (crest voltage 1390 kV)

Table 4: Combination 3 breakdown parameters

Combination	Δt μs	u_+ kV	U^- kV	Number of shots	Number of breakdowns	$(T_B - \Delta t)_{min}$ μs	$(T_B - \Delta t)_{max}$ μs	U_B kV
3(*a*)	400	1382	1190	10	2	10	21	2222
3(*b*)	600	1365	1190	10	5	7	37	2096
3(*c*)	700	1353	1200	10	3	7	29	2233
3(*d*)	800	1340	1190	11	3	10	14	2250
3(*e*)	1000	1315	1195	10	2	12	36	2034
3(*f*)	2000	1205	1195	5	0	—	—	—
				56				

u_+ = instantaneous value at time Δt of positive impulse (crest voltage 1390 kV)

Table 5: Combination 4 breakdown parameters

Combination	Δt μs	u_+ kV	U^- kV	Number of shots	Number of breakdowns	$(T_B - \Delta t)_{min}$ μs	$(T_B - \Delta t)_{max}$ μs	U_B kV
4(*a*)	400	1382	995	11	7	16	50	2189
4(*b*)	600	1365	1095	10	6	8	27	2359
4(*c*)	800	1340	1095	9	6	30	57	2161
			1195	12	10	8	35	2400
4(*d*)	1000	1315	1150	4	3	20	114	2060
			1190	7	6	15	44	2304
				53				

u_+ = instantaneous value at time Δt of positive impulse (crest voltage 1390 kV)

of the positive and negative voltage components to the electric field inside the gap differ from each other throughout the gap. In any case, the conductive leader channels and the space charges affect significantly the field distribution in the gap.

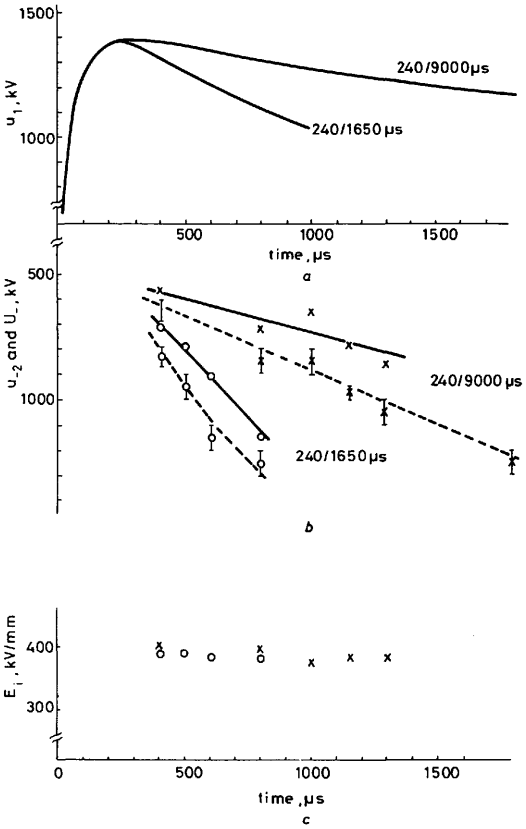

Fig. 2 *Plots showing the variation of the breakdown voltage*

a Positive impulse shape applied to the rod for creation of the original discharge
b Instantaneous inception voltage of the reactivation (solid line) and 50% breakdown voltage (broken line) for combinations 1 and 2
c Geometric field E_i at the cone tip at inception of the reactivation

The second factor is the evolution of the postdischarge processes during time Δt, for which two different and opposed effects have to be expected: the positive space-charge dissipation which is known to be characterised by a long time constant and which tends to make the reactivation easier as time progresses, and the decrease of leader conductivity which makes the reactivation more and more difficult.

In the present state of the work, it does not seem possible to separate these various effects. However, from a macroscopic point of view, it can be seen in Tables 2 and 3 that the total breakdown voltage U_B increases significantly when Δt is increased. The results which will be presented in this paper give the basis for thorough study of the causes of these variations.

2.2 Effect of impulse shape

The influence of the shape of the negative impulse can be discussed on the basis of Tables 2, 4 and 5 which refer to the same positive impulse (240/9000 μs). Even if the number of shots was rather limited, it can be observed that qualitatively the influence of the shape of the negative impulse on breakdown probability is in accordance with existing knowledge, which foresees an increase of withstand voltage when either front or tail duration of the impulse is reduced [1]. As an example, in the range 400 μs < Δt < 800 μs, the 50% negative crest voltage for breakdown is around 700–800 kV for the 40/165 μs impulse, 900–1100 kV for the 2/150 μs impulse, and well above 1200 kV for the 2.5/30 μs impulse. However, in the present experiment, it has to be noted that the initial conditions are not as controlled as in the usual studies of large airgaps. Variable preconditions already exist in the gap and will be interpreted in the following to be the main reason for the scatter observed in the results.

3 Characteristics of reactivation

Fig. 3 shows, for three different values of Δt, time-resolved image-convertor pictures of the light output from the discharge, together with simultaneously measured values of the electric field at the rod and at the plane, the current flowing and the computed apparent charge injected. The left sides of Figs. 3*a*–3*c* refer to the discharge developing during the positive impulse application to the rod (primary discharge), while the right sides show the records taken during the application of the negative impulse to the plane after a time delay Δt (reactivation of the discharge).

3.1 Basic leaders

The positive impulse applied to the rod at $t = 0$ caused a positive discharge to develop into the gap, which stopped after about 150–180 μs, i.e. before the crest value of the applied voltage was reached.

Generally two leaders developed simultaneously each having the characteristics typical of the positive leader development in long airgaps. These were extensively studied by this Group in the last decade [2–4].

When the negative voltage, applied to the plane after a time interval of Δt, reached a value u_{-2}, at time $t = t_2$, new ionisation phenomena occurred which propagated so as to follow the path of one of the previous leaders which was thus reactivated. This reactivated leader will be referred to as the 'basic leader' whereas the other, if it existed, will be referred to as the 'nonreactivated leader'. In all the cases where a leader was observed during the application of the second impulse, it invariably originated from a basic leader. No entirely new leaders were observed. This does not mean that such an event is impossible, because it can be anticipated that with a lower amplitude of the first impulse (and, consequently, a reduced propagation of the basic leader) and, with longer delay Δt for the application of the second impulse, such phenomena would appear. Let us first concentrate on Fig. 3*b*, which allows the main phases of the discharge to be identified, which will subsequently be represented as a sketch in Fig. 4. In this image-convertor picture, a leader, developing almost in the axial direction during the first phase, can be clearly seen. Another leader developed in the radial direction and cannot be clearly resolved. The phenomenon stopped after approximately 150 μs, as can be seen from the current oscillogram whose pattern during this phase is typical of a positive discharge.

The total measured charge Q_1 of approximately 100 μC corresponds well to a value of 50 μC/m, for the approximately 2 m overall combined length of the basic and non-

reactivated leaders. We will call L_{1b} and L_{1nr} their real lengths at the end of continuous propagation (the axial lengths being denoted Z_{1b} and Z_{1nr}). If they end through a restrike (i.e. a reillumination of the leader path accompanied by an extension of its length and a large current pulse), their overall length, which may differ from L_{1b} and L_{1nr}, will be noted L'_{1b} and L'_{1nr}.

Owing to the space charge injected by both leaders, the field at the plane (Fig. 3*b*) increases to the value E_1 until the phenomenon stops. By subtracting the electric field due to the applied voltage from E_1 the net space-charge field X_1 can be obtained. It can be seen that the space-charge field remains almost constant during the time interval Δt, indicating that the effect of both movement and recombination of space charge is negligible.

This fact is confirmed by the electric field measurement

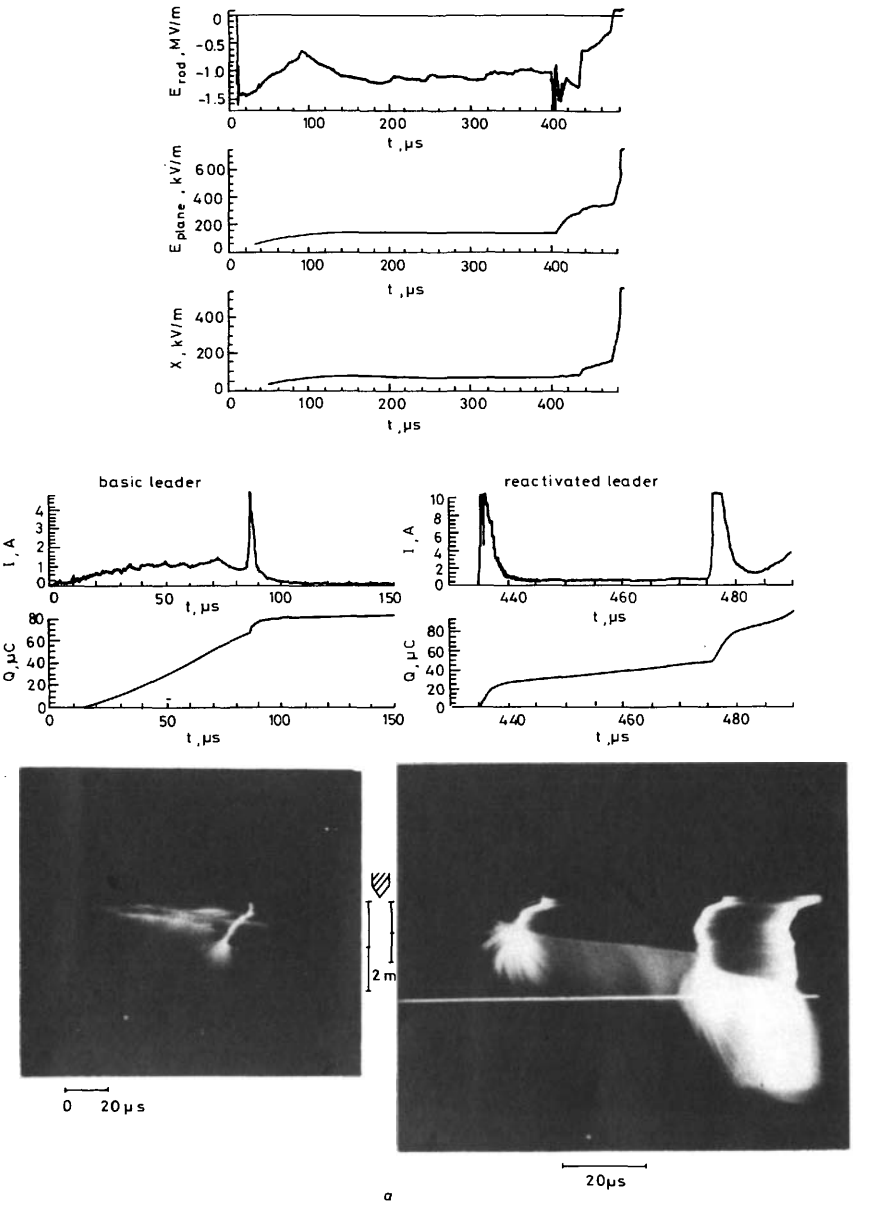

Fig. 3 *Typical records (total field at the rod, total and space charge field at the plane, current and injected charge, image convertor pictures) for three different configurations*

a Combination 1(*a*) $\Delta t = 400\ \mu s$, *b* Combination 1(*c*) $\Delta t = 1000\ \mu s$
c Combination 1(*f*) $\Delta t = 1300\ \mu s$

at the high-voltage electrode (Fig. 3*b*). This field first increased to a maximum α, then decreased continuously due to the effect of the space charge. Following the termination of the primary discharge growth β, the field then

increased, due to the rise of the applied voltage, until the crest value was reached γ. The subsequent slow decrease is due to both the reduction of the geometric field during the tail of the applied voltage and to minor ionisation activity, the effect of which could not be detected in the field measurement at the plane. These phenomena which repeat almost periodically are accompanied by faint periodic reilluminations of part of the channel and by small current pulses.

It has to be mentioned, however, that the field variation during Δt is of the order of only a few per cent of the total variation of the field due to the space charge.

3.2 Reactivated leaders

The reactivation of the basic leader proceeds through different phases, A, B, C and D, which are described below on the basis of the typical shot of Fig. 3*b* and the sketch in Fig. 4. Within some microseconds of the application of the negative impulse, a small current was observed. It corresponds to ionisation phenomena which are hardly visible

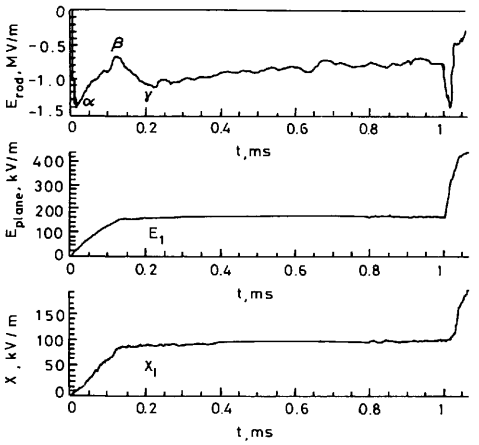

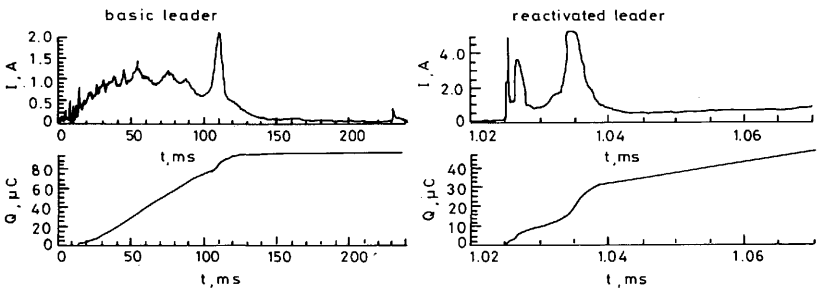

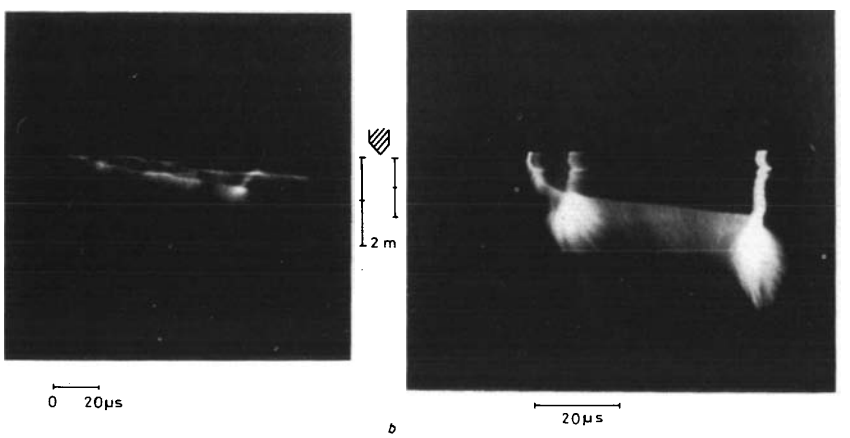

on the image-convertor records. Given the spatial resolution of these records, it is impossible to know whether these phenomena are related to the basic leader or whether they develop in virgin air. Then the reactivation process started at time t_2 through the reillumination of a part (Z_{2A}) of the basic leader. The reillumination developed almost instantaneously (in some hundreds of nanoseconds) from the rod to the length Z_{2A} accompanied by a small charge injection. This we define as phase A. The elongation of this second leader then continued at a velocity which was higher by about one order of magnitude along the channel of the basic leader, with a small leader corona at its tip (phase B). Sometimes, during phase B, weak restrikes could occur. When this second leader had

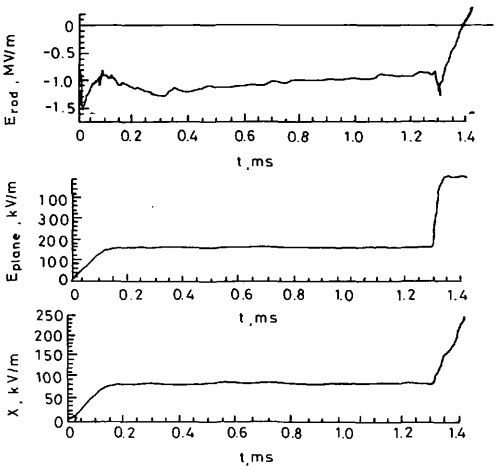

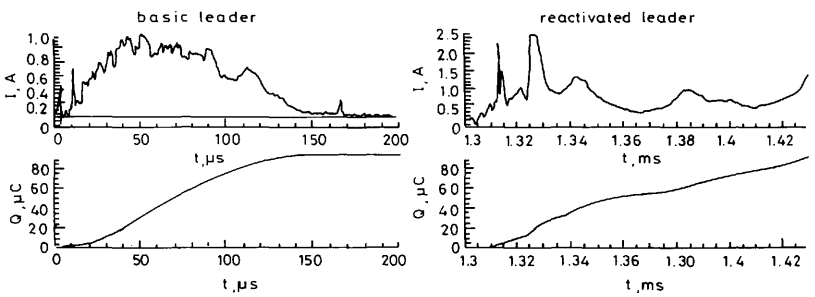

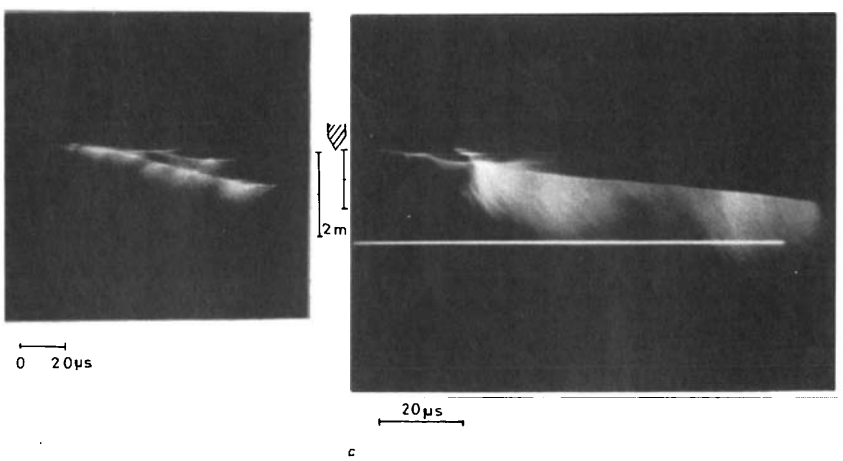

c

almost reached the end of the channel of the basic leader, some midgap ionisation phenomena were observed. The location of these events corresponded to the final position of the leader corona of the basic leader, but they were slightly more developed into the gap and were not linked to the tip of the leader. This midgap corona is clearly visible in Fig. 5, but generally it was masked by the intense corona which followed soon afterwards.

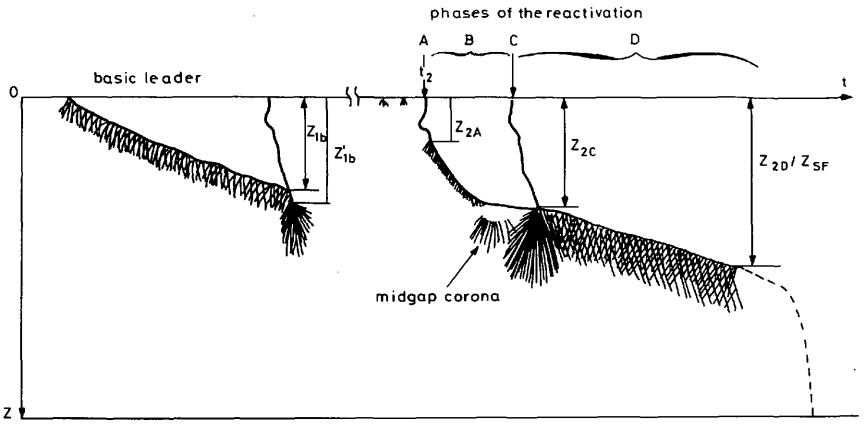

Fig. 4 *Sketch of an image convertor picture showing the different phases of the reactivation of a basic leader (the nonreactivated leader is not shown)*

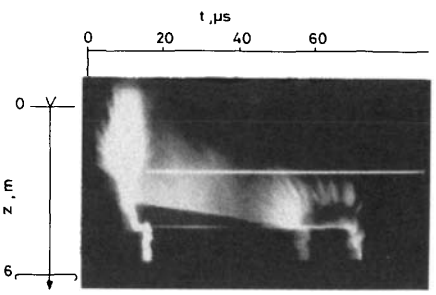

Fig. 5 *Example illustrating the midgap corona*
Combination $I(c)$: $U^- = 890$ kV

Phase B is defined as ending when the reactivated leader reached the tip of the basic leader. At that time, there was a bright reillumination of the whole channel accompanied by an intense leader corona. This brief event is phase C, which was followed by a leader propagation which continued in the usual way until the final jump, and is here called phase D. If a comparison is made with the basic leader development in Fig. 3, it can be seen that only phase D (and later on the final jump) behaves in the way normally associated with impulse leader development in long airgaps.

The first peak of current (Fig. 3*b*) corresponds to phase A, whereas the second peak corresponds to the faint reillumination of the channel during phase B which ends with the large current pulse due to the strong restrike (phase C). During phase D, the current remains almost constant at approximately 0.5 A.

From the static and image convertor records, a four dimensional (x, y, z, t) reconstruction can be made. The real leader length L as well as the velocity of the leader tip v are thus deduced and a framing sequence of the leader channel growth can be reconstructed as shown in Fig. 6 for the three shots presented on Fig. 3. This technique allows for direct comparison of the basic leader path (on the left side of each diagram) with the leader path during reactivation.

It should be noticed that all the phases A, B, C and D described in this Section were not necessarily observed in every shot. As an example, it can be seen in Figs. 3 and 6 (*a* and *c*) that the longer the delay, the shorter was the distance travelled during phase A, and, as a consequence, the longer was phase B (both in time and distance travelled). In other words, phase B tends to disappear for short Δt and phase A disappears for long Δt. Furthermore, it should also be noted that the examples displayed by Figs. 3 and 6 must be considered as typical examples representing an average of the observations made for a given Δt. It will be shown in the following that the available results are widely scattered.

4 Charge and field characteristics

4.1 Charge measurements

In Fig. 7, the charge injected during the reactivation is shown as a function of the real leader length for the typical three shots (with the different delays Δt already illustrated in Figs. 3 and 6).

It can be seen that, independent of the distance travelled during phase A (L_{2A}), the charge injected during this phase was practically negligible. Thus, the reactivation can be considered as a new leader starting from an advanced position with respect to the rod (L_{2A}), with a fast elongation during phase B along the old channel, accompanied by a small streamer activity until the old leader tip is almost reached. In this phase, the charge injection was around 10 μC/m. Then, the leader propagated in virgin air with the normal characteristics of leader propagation (phase D). It can be noted in Fig. 7 that, once phase D starts, the charge injection per unit real length is almost constant, with a value of 40–50 μC/m in all these cases.

In Fig. 8, the total measured charge Q_2 for a large number of shots is reported against the axial distance travelled by the new leader ($Z_2 - Z_{2A}$) in case of withstand. According to the way in which the discharge develops, two regression lines can be drawn, one for leaders ending at phase D and the other for leaders ending at phase B (or C).

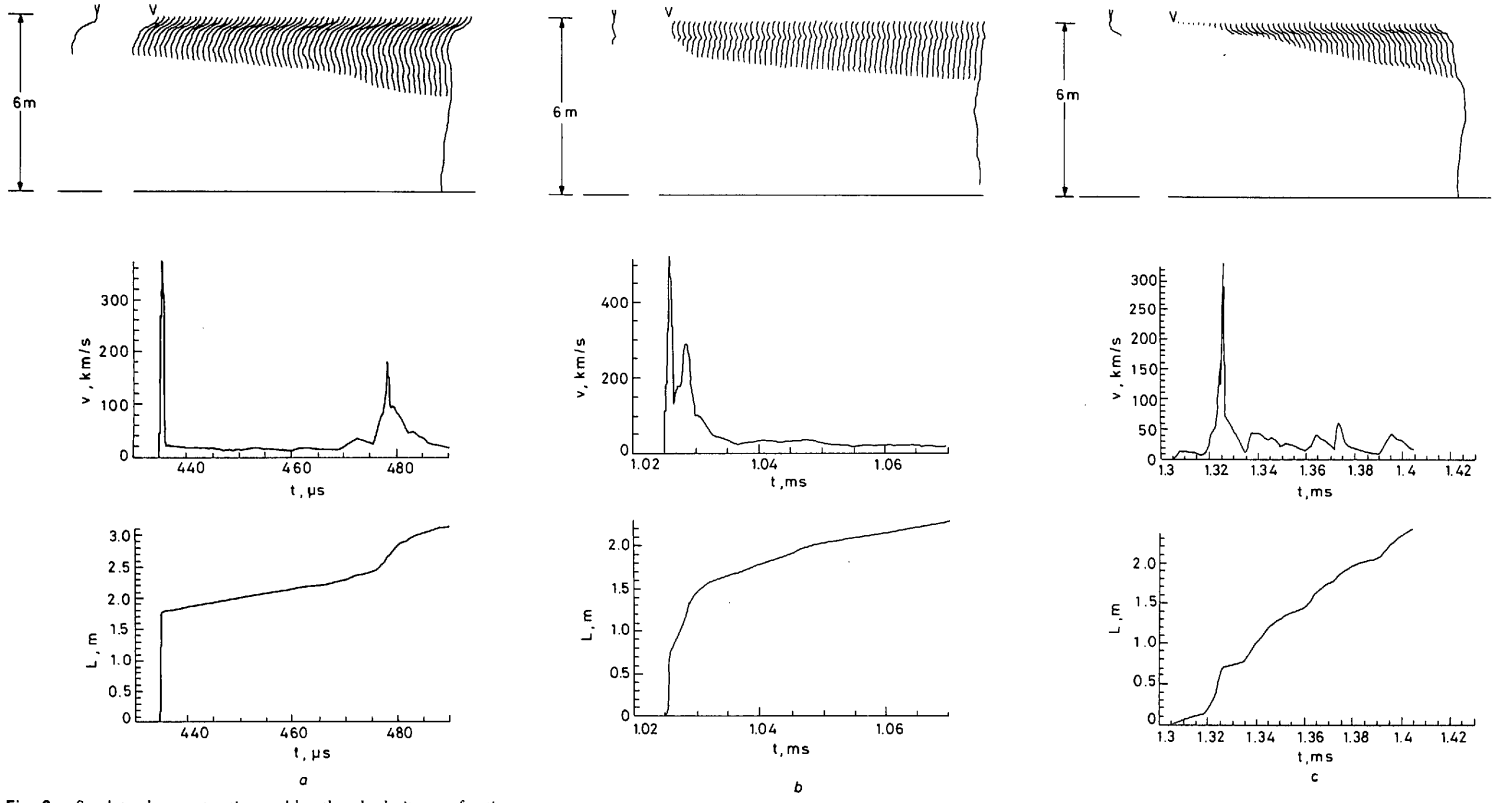

Fig. 6 *Spark track reconstruction, real length and velocity as a function of time for the shots illustrated in Fig. 3*

a Combination 1(*a*) $\Delta t = 400\ \mu s$
b Combination 1(*c*) $\Delta t = 1000\ \mu s$
c Combination 1(*f*) $\Delta t = 1300\ \mu s$

The two lines do not cut the Q_2 axis at the origin because of the presence of the charge injected during the previous phases.

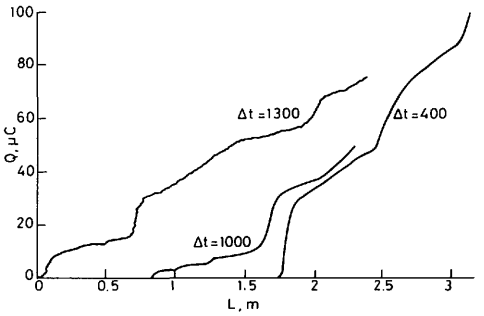

Fig. 7 *Variation of the injected charge as a function of real leader length for the shots illustrated in Figs. 3 and 6*

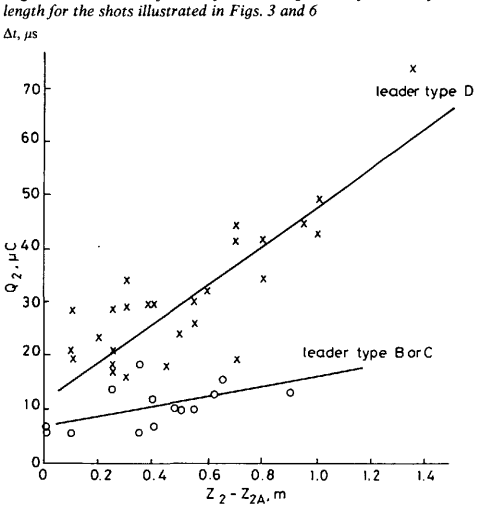

Fig. 8 *Total charge Q_2 injected by the reactivation process for withstand cases*

Combination 1
○ Partial reactivation of the basic leader (type B or C)
× Total reactivation of the basic leader followed by a further propagation (type D)

The slopes of the two lines, 40 μC/m and 10 μC/m approximately, represent, in practice, the average charge per unit length associated to phases D and B, respectively. Even if Fig. 8 refers to integral values of both charge and length, these results are in good agreement with those of Fig. 7.

It has to be mentioned that, if only phase A appears, a very small charge injection is measured, up to 5 μC, and its magnitude is independent of both the delay Δt and the applied voltage U_-.

4.2 Space-charge field

The total field strength E measured at the field probes L, J, D etc. in the plane electrode contained a significant component arising from the applied field G; this component was particularly large when the plane electrode was subject to the second impulse of peak voltage U_-, as shown by the field computation of Fig. 2*b* in Part 1. However, digital data processing, employed during the analysis of the records of the type shown here in Fig. 3, allowed the space-charge component X to be obtained by subtraction of G from E. The maximum values of the space-charge field change which occurred during the basic discharge growth and during the reactivation process could thus be obtained; X_1 and X_2 represent, for a given impulse, the mean values of the space-charge field change at the three field probes for these successive events. For the basic positive discharge, a large degree of proportionality is observed between the mean space-charge field X_1 at the plane and the measured charge flow Q_1 associated with the discharge. This is indicated by the lower family of grouped points in Fig. 9. In contrast, there is no evidence of proportionality for the reactivated discharge. The ratio X_2/Q_2 for this event varied greatly from impulse to impulse, and for some reactivations can be of an order of magnitude greater than X_1/Q_1 for the corresponding preceding basic discharge. The large range of X_2/Q_2 values of Fig. 9 is partly due to the wide range of controlled parameters U_- and Δt, which were used. However, much of the variation is due to the uncontrolled variables of the basic discharge and to the different types of discharge reactivation which have been described in Section 3.2. Any modelling of basic and reactivated leaders would need to take account of the contrast shown by Fig. 9.

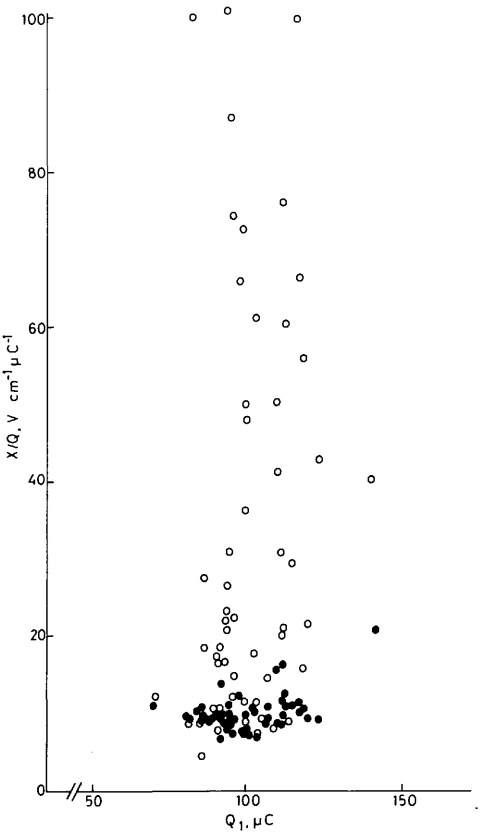

Fig. 9 *Comparison of basic and reactivated discharges*

Space-charge field per unit charge flow.
● X_1/Q_1 basic discharge. U^+ 1390 kV 240/9000 μs
X_1 = mean space-charge field for probes L, J, D
Q_1 = measured charge flow
○ X_2/Q_2 reactivated discharge 40/165 μs
U^- 505 kV, 1200 kV; Δt = 400 μs, 1800 μs

5 Influence on the reactivation process of the controlled parameters

It was already pointed out that, during the application of the first impulse, two leaders usually develop simultaneously in directions which often diverge widely from the gap axis. This is probably due to the very highly divergent applied electric field resulting from the electrode geometry used, i.e. $R/D \approx 10^{-4}$ (see Appendix 10.1). These two leaders develop in a very random way. Usually of different length (which varied in a wide range from 30 to 250 cm), they may or may not be found to end their propagation with a restrike.

Thus, the initial conditions of the leader reactivation which occurred during the application of the second impulse were determined not only by the controlled parameters (i.e. the shape of the first impulse, the time delay Δt, the crest value and shape of the negative impulse), but were also greatly influenced by the development of the leaders of the original discharge (i.e. the distance travelled, the amount of charge injected and its position in the gap, whether or not terminated with a restrike), which were uncontrollable parameters.

In spite of the great number of tests performed the scatter of the results is quite large and the influence of the controlled parameters is to a great extent masked by the great variability of the uncontrollable parameters.

Furthermore, even if the uncontrolled parameters in different discharges appear to be the same, the reactivation process may be totally different, as can be seen in Fig. 10. This example, obtained for $\Delta t = 1000\ \mu s$ and $U_- = 900$ kV, shows two successive shots with a 4 min interval. In both cases, the basic leader was well developed and nearly on the gap axis. In both cases, the leader ended with a strong restrike and the associated charge Q_1 was similar. However, in one case, the negative impulse caused a reactivation followed by breakdown, and in the other case, no significant reactivation was observed. This example illustrates the fact that a complete comprehension of the problem would necessitate a larger series of tests.

5.1 Negative crest voltage

It is clear from the results that, for a given value of Δt, U^- has to be high enough to provoke the reactivation at time t_2. As an example, for the combination 1.1 ($\Delta t = 400\ \mu s$ and $U_- = 505$ kV) (Table 2), the reactivation at time t_2 occurred in two cases out of seven and for combination 1.3, U_- had to be increased up to 690 kV to obtain the reactivation in three cases out of ten. When U_- was increased above these values reactivation occurred in every case. This clearly demonstrates the existence of a threshold. Above this threshold, it was observed that the average inception voltage u_{-2} showed no clear relationship with U_-. This is due to the small number of shots performed, which consequently does not allow a precise statistical analysis, and also to the limited range of U_- values which were investigated.

Following the inception of the reactivation, it is possible to discern the effect of U_- on leader growth and the probability of breakdown. Fig. 11 gives, for different values of U_-, the phase at which the discharge stops in case of withstand and the time to breakdown in case of breakdown. It can be seen that, when U_- was increased, the number of discharges which did not reactivate decreased, while those which reactivated developed progressively further towards phases B, D and breakdown. Furthermore, the average time to breakdown decreased.

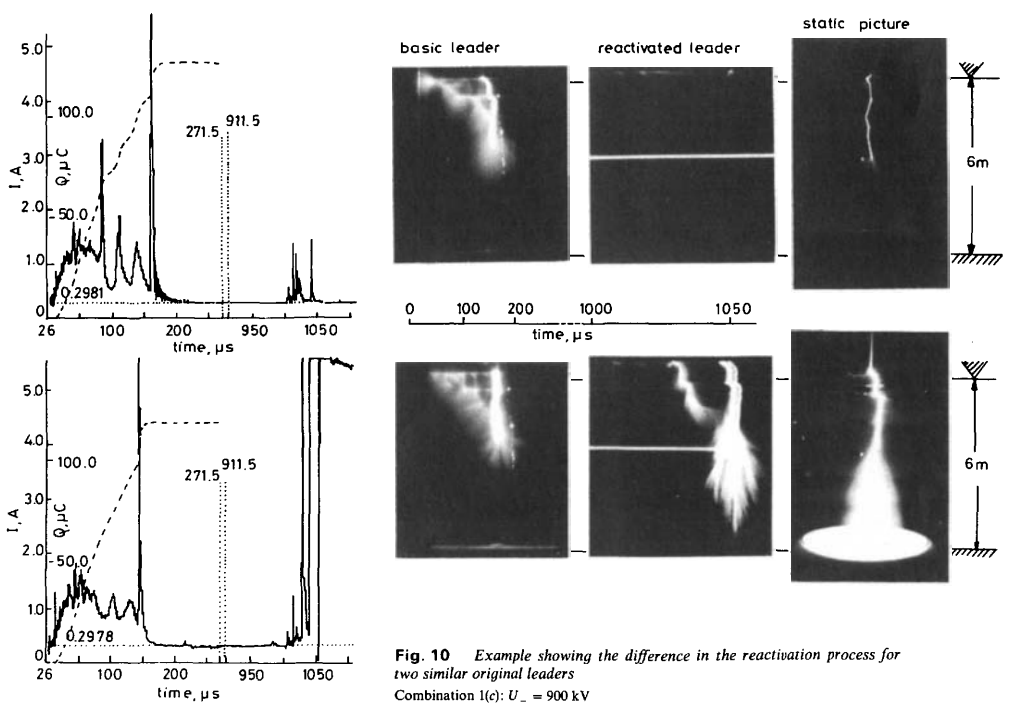

Fig. 10 *Example showing the difference in the reactivation process for two similar original leaders*
Combination 1(c): $U_- = 900$ kV

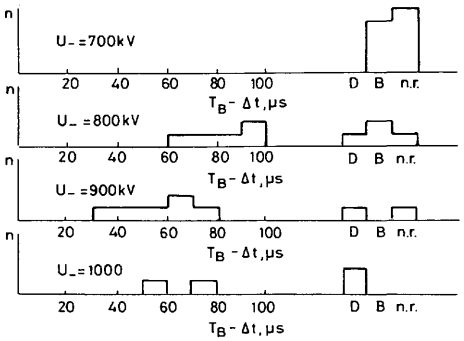

Fig. 11 *Influence of U_- on the phase (n.r. = no reactivation; B, D or breakdown) reached by the reactivation process for combination 1(c)*

5.2 Negative impulse shape

When the shape of the negative impulse was modified during the tests, the reactivation process and the breakdown probability were changed in consequence. Steeper negative fronts were used in combinations 3 and 4 (Table 1). With such impulses, the main qualitative result was that phase B disappeared completely. Instead, when the reactivation occurred, phase A always extended to the tip of the basic leader so that the general structure described in Fig. 4 became much simplified. The reactivation process was more violent and, in a significant number of cases, the large corona associated with phase C extended to the plane. Fig. 12 is an example for combination 3 which, it should be noted, was a withstand case (the image-convertor shutter was not operated). Additionally, the 'midgap corona', as described in Section 3, was clearly visible in the region which had been occupied by the streamers of the basic leader corona.

For combination 3, where the tail of the negative impulse was very short, the development of the discharge to the stage where corona reached the plane did not necessarily lead to breakdown. This is a classical result, typical of impulses with short tails. For combination 4, where the tail was longer, such a phenomenon became less frequent, but could still be found.

For both combinations, the probability for reactivation and for breakdown can be related to the well known idea that the voltage has not only to be high enough, but in addition has to exist for a time long enough to allow full development of the discharge.

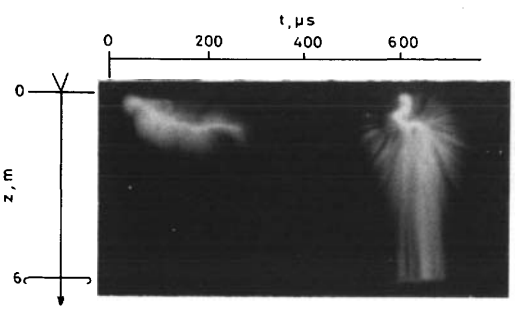

Fig. 12 *Original discharge and reactivation for combination 3(b)*

5.3 Time delay between positive and negative impulses

5.3.1 Influence on the reactivation inception: Whereas no clear correlation could be found between the inception voltage u_{-2} for reactivation and the crest voltage U_-, a correlation was observed with the time delay Δt. This variation, which was shown in Fig. 2, exhibits a trend similar to that of the breakdown voltage.

It may be due either to the movement and recombination of the space charge during Δt or to the variation of the positive voltage applied to the rod. The relative importance of these two effects can be discussed as follows:

(i) In part 1, it has been shown that a given applied voltage created a field at the cone tip which was 2.7 times higher when the voltage was applied to the rod than when it was applied to the plane. In Fig. 2*c*, the effect of both voltages have been combined so as to show the variation of the field at the cone tip as a function of Δt. It can be seen that this inception field is roughly constant and depends neither on Δt nor on the shape of the impulse tail.

(ii) As already mentioned in Section 3.1 the field measurements at the tip and at the plane did not show any significant variation during Δt. This indicated that drift and recombination of the space charge during this period was rather limited.

As a consequence of these two remarks, it can be concluded that, in the range of Δt which was investigated, the characteristics of the leader decay had a very small influence on the reactivation inception which seemed to be determined by the value of the electric field at the cone tip which had to be reached to allow ionisation to become effective.

5.3.2 Influence on the reactivation length: According to the above, the influence of Δt on the reactivation voltage u_{-2}, shown in Fig. 2*b*, is more a consequence of the variation of the positive applied voltage rather than of a significant variation of the characteristics of the medium in the proximity of the tip from which reactivation starts.

On the contrary, the time delay Δt has a clear influence on the characteristics of the reactivation, giving useful information on the way in which leader decays. Fig. 13 gives the real length L_{2A} of the reactivated part during phase *A* as a function of Δt; despite the large scatter, it can

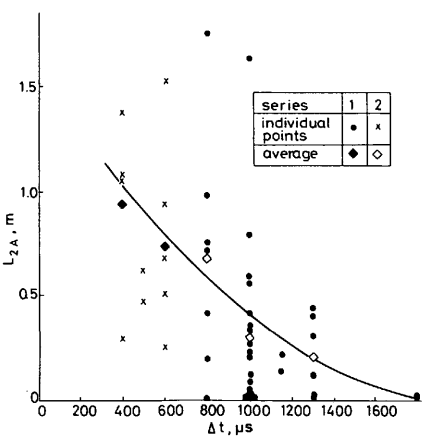

Fig. 13 *Variation of real reactivated length L_{2A} as a function of Δt for combinations 1 and 2*

be seen that on average L_{2A} decreases significantly with increasing Δt. To take some account of the variability of the basic discharge, the relative axial length which is reactivated during phase A is plotted as a function of Δt in Fig. 14. The average reactivated length decreases with Δt, and this decrease is not significantly affected by the tail duration of the positive impulse.

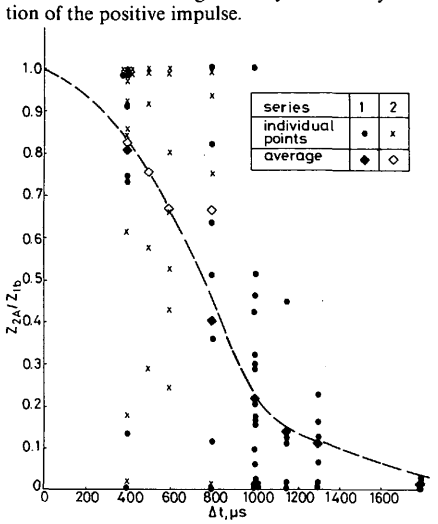

Fig. 14 *Variation of the relative axial length Z_{2A}/Z_{1b} as a function of Δt for combinations 1 and 2*

This type of result indicates that the characteristics of the basic leader are changing with time, beginning at the tip of the leader itself, and these changes gradually extend towards the older sections near the base of the leader. This behaviour is in agreement with models previously developed for the local characteristics of a leader: the conductivity of a leader channel is not uniform along its length, and the older sections of the channel (which have been submitted to current flow for a longer time) are more conductive, so that it could be expected that the recovery of the initial conditions is reached first in the younger sections where the modifications of the medium are less pronounced.

The fact that the behaviour of Fig. 14 does not depend significantly on the tail duration of the positive voltage would indicate that the recovery of the initial characteristics is not greatly affected by the applied electric field but is mainly governed by thermodynamic processes and/or the space-charge field. From both Figs. 13 and 14 it can be seen that the scatter of the results is quite large. It may be noticed, as an example, that for $\Delta t = 400$ μs the majority of basic leaders are reactivated during phase A over their whole length, but some are not reactivated at all. On the contrary, for $\Delta t = 1000$ μs, most of the discharges are reactivated only over a short portion, but it is still possible to observe a complete reactivation of the basic leader. The physical reasons which cause the large scatter in reactivation lengths during phase A have not yet been clarified. However, on average, the value of Δt, for which reactivation of one half of the basic leader occurs during phase A, lies in the range of 600–800 μs. It has to be kept in mind that this value refers to basic leaders of 1 to 2 m length with an associated charge of 50–100 μC. It would be expected that this characteristic time would depend on the length of the basic leader, i.e. on the type and duration of its propagation.

6 Influence of the original discharge

The complexity of the reactivation process is well illustrated by examining relationships between the characteristics of the original discharge and the characteristics of the reactivation process, the controlled parameters being fixed. Fig. 15 gives the relationship, from a shot by shot analysis, between the reactivated length Z_{2A} at phase A and the length of the basic leader Z_{1b}. Apart from the trivial result that breakdown is easier if the ratio Z_{2A}/Z_{1b} is larger, no clear relationship can be found.

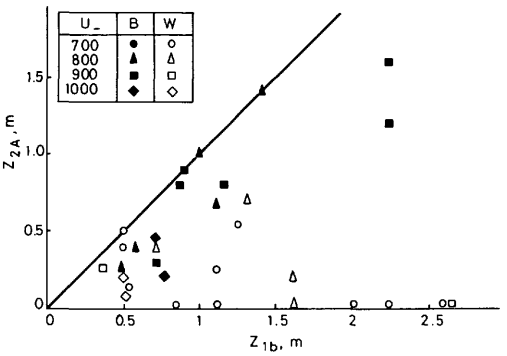

Fig. 15 *Axial reactivated length at phase A, Z_{2A}, as a function of the axial length of the basic leader Z_{1b}*
Combination 1(c)

Despite the great variability of its characteristics, some effects of the original discharge can be identified. In particular, it was observed that the reactivation process after the inception was greatly influenced by whether the longer or shorter leader was reactivated and whether that basic leader had terminated with a restrike.

Based on the observation that there was one long and one short leader, that either may or may not end in a restrike, and that only one is reactivated, the tests can be divided in 4 groups as shown in Table 6. In turn, each group gave rise to the reactivation of the longer or shorter leader with a relative frequency which is listed in the same Table.

Table 6: Reactivated leader as a function of the original discharge characteristics

Primary leaders	Total	Reactivation (Rel. %)	
		long	short
	%	%	%
Both with restrikes	3.7	100	0
Both without restrikes	42.6	80.5	19.5
Restrike long only	42.6	76	24
Restrike short only	11.1	100	0

It is noticeable that a shorter original leader was never reactivated if it terminated with a restrike.

Apart from these cases, which represent only 15% of all the cases, the shorter original leader was reactivated in a significant number of cases (22%) and this proportion did not depend on the way in which the longer leader ended its propagation.

Fig. 16 shows a typical example where the basic leader was shorter than the non-reactivated one.

However only 6% of the short basic leaders led to breakdown. The significant amount of shorter leaders reactivated is probably due to the fact that the inception of reactivation depends, as discussed here, on local conditions

near the electrode. These conditions are obtained after Δt mainly because of the increase of the geometric field, which

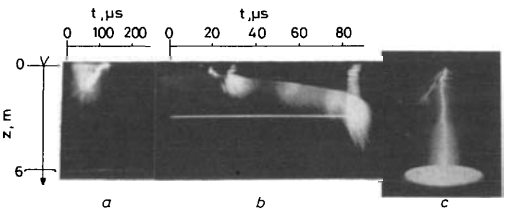

Fig. 16 *Example showing the reactivation of the shorter original leader*
Combination 1(*b*): $U_- = 800$ kV
a Original discharge; *b* Reactivation; *c* Static picture

does not depend on charge distribution. On the contrary, its subsequent propagation is inhibited by the shielding effect of the positive space charge of the much longer non-reactivated leader, which was left in a more advanced position with respect to the point electrode.

The case of longer leader reactivation is the more frequent, probably because the inception conditions at its base, which is normally 'older' and more conductive, are reached first when the negative voltage is applied.

In this case the subsequent process is greatly influenced by whether the basic leader had ended its propagation through a restrike. If this had occurred, and phase D was reached, almost always (34 times out of 36) the discharge ended with breakdown.

Furthermore, it is generally observed that, in these cases, the new leader does not follow the whole length of the old channel, but deviates without using the last part created during the restrike (Fig. 17). This behaviour can be explained by the fact that a restrike is always accompanied by a large space-charge injection at the tip which partially prevents new streamer formation and propagation, so inhibiting phase D.

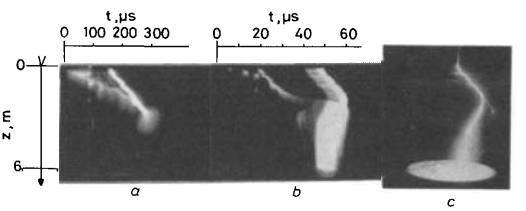

Fig. 17 *Example showing that when the original leader ends through a restrike, the basic channel is not completely reactivated*
a Original discharge; *b* Reactivation; *c* Static picture

If, however, the leader can continue its propagation, avoiding this zone of space charge, its position becomes so advanced that breakdown cannot be easily avoided.

7 Strioscopic analysis

The strioscopic equipment used during the tests have been described in part 1. The region of the discharge which could be analysed was restricted by the optical field of view to some centimetres in the vicinity of the rod tip.

Fig. 18 shows an example of the strioscopic images of the channel which were successively recorded some microseconds before, 20 μs after and 30 μs after the application of the negative impulse. In other words, the first image shows the state of the basic leader which has decayed; the second is taken after the application of the negative impulse but before the beginning of the reactivation; the third one shows the channel after phase A of the reactivation. The main deduction from this sequence is that,

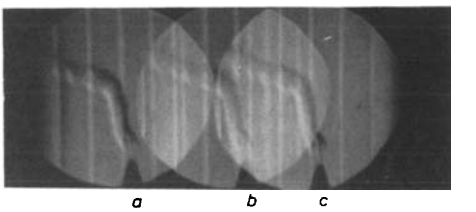

Fig. 18 *Strioscopic picture of the channel near the rod at times 1780 μs, 1820 μs, 1839 μs*
Combination 1(*f*): $\Delta t = 1800$ μs

apart from a zone very near the rod, the channel diameter was not modified by the reactivation.

Fig. 19 gives a set of four strioscopic images taken after the inception of the reactivation process (phase A) for different values of Δt. As previously shown in Fig. 18, these images are representative of a leader which has decayed during a time Δt. It can be seen that, with increasing Δt, the channel diameter became larger, the contrast between the dark and light sides of the channel decreased and the edges of the channel were less and less well defined. The increase of the channel cross-section is given as a function of time in Fig. 20. During the phase of positive leader propagation (about the first 200 μs) the leader diameter increases quickly, as is already known [4]. Then, the expansion rate of the channel decreases. This is a phase during which the expansion is due only to thermal expansion, where heated gas molecules tend to leave the channel and are cooled, and cold gas molecules diffuse into the hot channel. This causes a lower density gradient at the leader channel boundary and a less sharp image. For the same reason, the diameter of the hot channel increases and the temperature inside the channel decreases, and, with a constant pressure expansion, the channel gas density increases

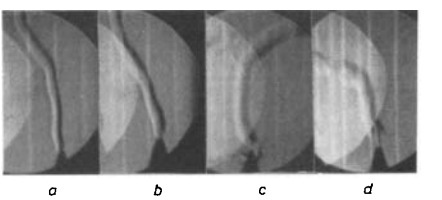

Fig. 19 *Comparison of the strioscopic image of the channel after the reactivation (Δt + 30 μs) for different values of Δt*
a 400 μs; *b* 600 μs; *c* 1150 μs; *d* 1800 μs

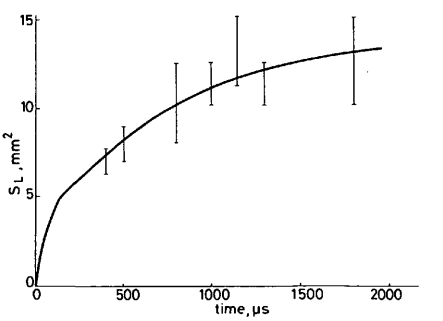

Fig. 20 *Variation of the section of the original leader as a function of time*

towards the density of the surrounding gas resulting in the observed decrease in the contrast of the channel.

Let us consider now the zone very close to the rod in Fig. 18. In the first picture, the channel is no longer visible. This suggests that, in this region, the gas has returned to its original state. The implication is that the cooling process in the vicinity of the rod is much more efficient than further into the gap. This is mainly due to the high thermal conductivity of the rod and local convection.

It can also be seen in Fig. 19 that, as might be expected on the above grounds, an extension of this zone occurs with time. It may be surmised that the local temperature in the sections closest to the rod has dropped to a very low level compared with the temperature of the other sections, and the local density is much higher. Although the decay process in these sections is then practically complete, the reactivation causes a very narrow channel to appear, which then joins the leader channel to the point electrode (Fig. 18*c*). This narrow channel might be the strioscopic appearance of the weak corona activity which occurred, as already described in Section 3.2, at the rod tip before the beginning of phase A.

8 Conclusions

These tests have successfully identified the effect of a pre-existing leader channel on the breakdown strength of a 6 m airgap. The processes observed in the reactivation of such a channel allow both a physical study of the decay of the leader channel and an engineering guide for insulation co-ordination purposes of treating independently two successive surges.

The decay of a positive leader channel which stopped its propagation has been studied by examining its behaviour when the gap is restressed after variable time interval Δt.

(*a*) During time Δt minor ionisation phenomena occur, associated with faint reilluminations of part of the leader channel. In general, the light emission of this phase was too poor to be examined in detail.

(*b*) When the restressing is applied, the channel is reactivated and this reactivation process appears to be influenced both by the characteristics of the initial discharge, which have been referred to here as the uncontrolled parameters, and by the controlled parameters of the reactivating voltage and its time of application:

(i) For a time delay of the order of 400 μs, the whole channel of the basic leader was suddenly reactivated. The charge injection corresponding to this reactivation is very small. The propagation of the leader than continued, presenting the general characteristics of the standard positive discharge in long airgaps: leader velocity of 1.5 cm/μs, injected charge of 50 μC/m.

(ii) For time delay of 1800 μs, the process started from the electrode without any sudden reactivation. However, the channel followed by the new leader was the basic leader path. This indicated that even if the conductivity of the channel was highly reduced its temperature remained significantly higher, and the gas density significantly lower, than in the surrounding gas.

(iii) For intermediate values (1000 μs), only a part of the basic leader was reactivated with little charge flow. The remaining part of the basic leader needed a charge of about 10 μC/m to be reactivated. During this phase, the channel was reactivated through a very small leader corona at a velocity which was an order of magnitude higher than in the standard case.

These observations indicate that the recovery of the initial conditions is reached in the younger and more conductive sections of the leader near its tip.

(c) Leader reactivation took place always starting from the zone in the vicinity of the point electrode, and the inception voltage was such that the geometric component of the field at the tip electrode was almost the same, and independent of Δt.

(d) With steeper negative fronts the peak values had to be higher, and the sudden reactivation always progressed to the tip of the basic leader.

(e) The above conclusions are representative of an average event, but the scatter of the results is very large. The cause of this dispersion is considered to be due to the detailed characteristics of the propagation of the basic leader, i.e. the spatiotemporal evolution of the leader tip and the distribution of the space charge injected into the gap. In the present experiment, these characteristics were not resolved, in space and time, with a sufficiently high precision to allow definite conclusions to be drawn. However, some results are indicative of this interpretation, based on observations of which original leader, of the two normally present, was reactivated:

(i) The reactivated leader was the shorter one in a significant number of cases (20%).

(ii) The probability of reactivation of the shorter leader depended on whether or not the basic leader ended its propagation through a restrike.

(iii) When the long basic leader ended its propagation through a restrike, the channel created during the restrike was generally not reactivated, particularly where the restrike was strong; this was probably due to the choking effect of the large positive charge associated with the restrike.

(f) The strioscopic study of the discharge showed that the cooling of the channel was more efficient in the vicinity of the anode, where heat conduction played a decisive role. Further from the anode, the channel section increased with time through heat transfer at the boundary of the channel, whereas the channel temperature decreased.

(g) The recovery of an airgap in which a leader discharge has been created is governed by three characteristic times:

(i) The time characteristic of the decay of the leader channel conductivity. This time is of the order of 1 ms.

(ii) The time characteristic of the cooling of the leader channel.

(iii) The time characteristic of the space-charge dissipation.

These last two phenomena are characterised by times which are much longer than the time intervals used throughout the present experiment. Further studies would be necessary to clarify this question.

9 References

1 KIND, D.: 'Die Aufbanflache bei stossspannungsbeansprunching technischer electrodeanordnunger in Luft', *ETZ A*, 1958, **79**, pp. 67–69

2 LES RENARDIÈRES GROUP: 'Research on long air gap discharges at Les Renardières', *Electra*, 1972, (23), pp. 53–157

3 LES RENARDIÈRES GROUP: 'Research on long air gap discharges at Les Renardières: 1973 Results', *ibid.*, 1974, (35), pp. 49–156

4 LES RENARDIÈRES GROUP: 'Positive discharges in long air gaps at Les Renardières: 1975 Results and conclusions', *ibid.*, 1977, (53), pp. 31–153

5 DUPUY, J., GIBERT, A., DOMENS, P., HUTZLER, B., RIU, J.P., and EDLINGER, F.: 'Application de la strioscopie à l'étude du canal ionisé de l'amorçage en très haute tension', *RGE*, May 1981, pp. 399–407

6 ALLEN, N.L., CLARK, P., DRING, D., and WATERS, R.T.: 'Ionic combination and the estimation of the negative ion component in

positive corona', *in* 'Gas discharges and their applications' (University of Leeds Press, 1985), pp. 163–166
7 ALLEN, N.L., BERGER, G., and DRING, D.: 'Positive corona and atmospheric negative ion density under repetitive impulse conditions'. IEEE Summer Meeting, 1982
8 GALLIMBERTI, I.: 'The mechanism of the long spark formation', *J. de Physique, Colloque C7*, 1979, **40**, suppl. 7, pp. 193–250
9 GALLIMBERTI, I.: 'A thermodynamic model of the leader channel', *Electra*, 1977, **53**, pp. 89–97
10 POLI, E.: 'Positive corona inception under variable humidity conditions'. 8th Int. Conf. on Gas Discharges, Oxford, 1985
11 SOMERVILLE, I.C., and TEDFORD, D.J.: 'Time-lags to breakdown: the detachment of atmospheric negative ions'. 5th Int. Conf. on Gas Discharges, London, 1978
12 DUTTON, J.: 'A survey of electron swarm data', *J. Phys. Chem. Ref. Data*, 1975, **4**, pp. 577–856
13 GALLIMBERTI, I., HARTMANN, G., and MARODE, E.: 'The leader to spark transition', *Electra*, 1977, **53**, pp. 123–132
14 WALTY, J.R., WILSON, R.E., and WICKS, C.E.: 'Fundamental of momentum, heat and mass transfer' (Wiley, New York, 1969)

10 Appendixes

10.1 The development of double leaders in the positive polarity discharge

R. TURRI

10.1.1 Introduction: Positive leader development in long airgaps has been extensively studied [4], and it has been verified that the propagation tends to occur more or less along the electric field lines with an average injected charge per unit leader length of 40–50 μC/m.

In the current experiment on leader decay a very highly nonuniform electric field geometry was used, i.e. a 6 m point-plane gap D with a point radius R of 6 mm, which gives a ratio $R/D = 10^{-4}$. Thus the geometric field is extremely high in a relatively large sphere around the positive point (see the field computation reported in part 1) resulting in the inception of two primary leaders in the majority of the cases (more than 90%).

In all cases, however, only one of the two leaders is reactivated when the gap is restressed.

As indicated in Section 4.1, the presence of two primary leaders greatly influences the scatter of the results when investigating the reactivation of a channel, and thus it is of importance to understand fully the characteristics of the primary leaders' development. In the following, therefore, these characteristics are discussed, on the basis of electrical and optical measurements carried out during the experiment of this part.

10.1.2 Results and discussion: Fig. 21 shows the total charge injection Q_1 against the sum of axial lengths of the two leaders which we here call the total length. In this Figure two regions can be identified: namely, that where the total length is less than 2 m and the injected charge is greater than the usual 50 μC/m (represented by the dashed line) and that where the total length is above 2 m and the injected charge per metre has the usual value.

In this part it was observed that the simultaneous development of the two leaders always had one of the following characteristics:

(i) the two leaders had lengths of the same order and tended to develop far from the gap axis, due to the mutual repulsion of the positive space charge at their heads. Therefore, the real lengths were much longer than the axial lengths. From the static pictures taken from two different positions, they appeared to develop almost symmetrically, thus giving rise to a uniform electric field distribution over a wide area in the centre of the plane electrode.

(ii) one leader was much longer than the other with usually an inverse relationship between the two lengths. The propagation of the longer leader was nearer the axis than in (i) and it could reach distances of the order of 3 m in the case of withstand. The leader's development was no longer symmetrical and the shorter leader path could have a very wide angle with respect to the gap axis (quite often 90°).

From Fig. 22, in which the shorter leader length is plotted against the longer leader length, it can be seen that two leaders having comparable lengths can only propagate up to about 1 m axial distance. When the longer leader length is greater than 1 m, the shorter leader can have lengths up to a maximum value that is inversely proportional to the length of the longer leader. In this particular experimental arrangement, we find

$$Z_{Sh\,max} = 0.625(290 - Z_{Lo})\ \text{cm}$$

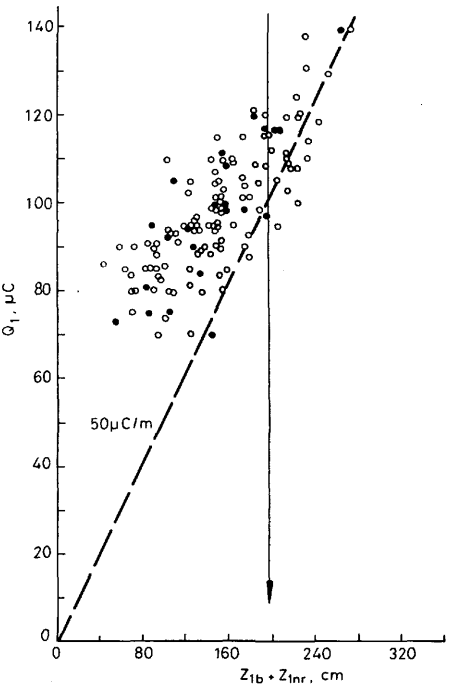

Fig. 21 *Apparent charge injection Q_1 as a function of the sum of the axial leaders' lengths $Z_{1b} + Z_{1nr}$*

○ data from combination 1
● data from combination 2

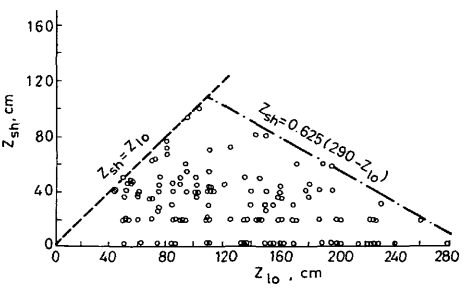

Fig. 22 *Shorter leader length Z_{sh} as a function of longer leader length Z_{lo}*

Data from series 1 and 2

where $Z_{Sh\,max}$ is the maximum axial distance of the shorter leader and Z_{Lo} is the axial distance of the longer leader.

In most cases, however, the shorter leader has an almost negligible propagation and thus does not influence the propagation of the longer leader. In fact, returning to Fig. 21, we see that for total lengths above 2 m the charge injection per metre is about 50 μC/m as usual.

A much higher charge injection per unit length is registered for lower total axial lengths, because the two leaders tend to be more equal in length and to develop much more off axis. Thus their real lengths are much greater than the axial lengths.

If, therefore, Fig. 21 were to be replotted with real lengths instead of axial lengths on the horizontal axis it is probable that the measurements would lie on the straight line corresponding to 50 μC charge injection per metre of real distance travelled by the leaders.

The probability of (i) or (ii) occurring was observed to be almost equal and it is most likely the difference between the inception times of the two leaders that determines their behaviour.

In Fig. 23 the electric field conditions which may appear in the anode region at different phases of the positive discharge are sketched. Fig. 23*a* represents the geometric field just before corona inception. The distorted field due to the corona streamers before the leader inception is shown in Fig. 23*b*. If now the two leaders start about at the same instant, their positive heads electrically repel each other so that they can only propagate at a large angle to the axis and have almost symmetrical directions (Fig. 23*c*). In a large number of cases, the observed angle between the two leaders was about 90°.

In cases where only one leader starts, it is likely to propagate more or less along the gap axis, where the geometric field gradient is highest, and it can travel much longer distances than when two leaders start simultaneously. Furthermore, the single leader completely changes the field distribution near its head and, more importantly, in the vicinity of its channel. The resulting equipotential distribution will then be something like that sketched in Fig. 23*d*. From the above we see that if a second leader is initiated after a fairly long delay, it can only propagate in almost a radial direction, i.e. at 90° to the longer leader, as shown by the arrows in Fig. 23*d*, and only for short distances because the field decreases very rapidly in the radial direction.

It may thus be said that, in both cases (i) and (ii), the two leaders tend to advance along perpendicular directions (at least in the first stages of their propagation), and this was observed in a large number of cases.

If we consider the energy dissipated during the process then, for the case where two leaders start simultaneously, there will be an about equal energy input to each channel, and, as the electric fields they encounter will be similar, they will tend to propagate approximately the same distance.

10.1.3 Conclusions: For the present highly nonuniform field geometry, two primary leaders were almost always initiated. Despite the mutual interaction between them,

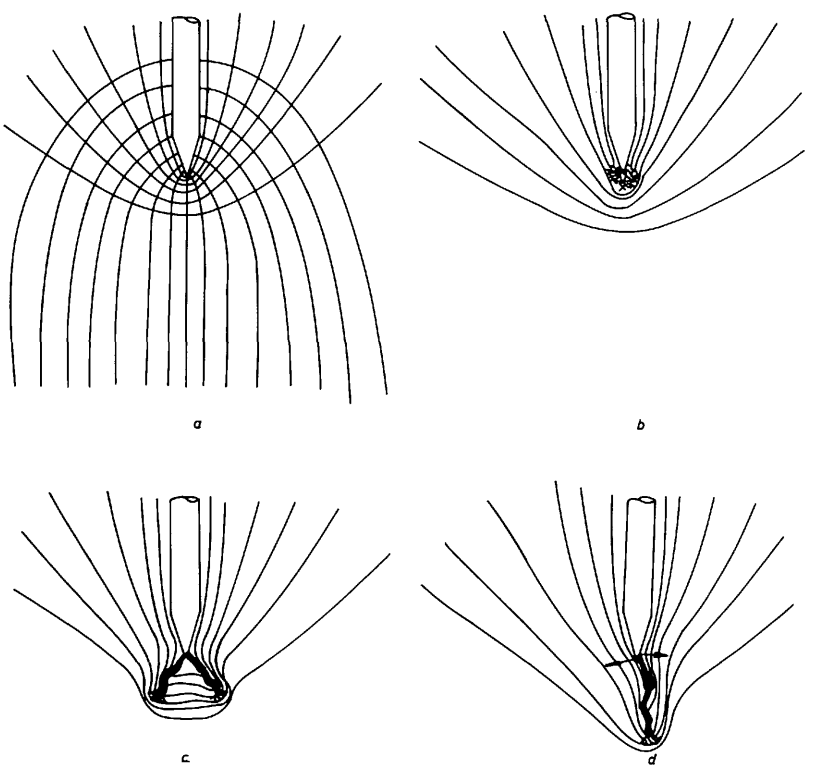

Fig. 23 *Electric field in the anode region at different phases of the discharge*
a Geometric field; *b* Distorted field due to corona; *c* Distorted field due to two simultaneous leaders; *d* Distorted field due to single leader

each of the two leaders appears to develop in the normal way already extensively investigated for long airgaps of positive polarity.

When one leader starts appreciably before the other, it has a large influence on the propagation of the second leader, because the electric field distribution is greatly distorted in the region of the anode. The first leader can travel an axial distance greater than 1 m, and the maximum final length of the second leader is observed to be inversely proportional to the length of the first leader. In most cases, however, the second leader only has a very limited propagation.

If, on the other hand, two primary leaders develop almost simultaneously, their influence is reciprocal, so that the propagation is largely off axis. The development of the two channels is almost symmetrical with respect to the gap axis and the leaders can reach axial lengths up to a maximum of about 1 m.

In both the above cases the channels of the leaders are appproximately perpendicular, at least in the early stages of the development.

The reasons why only one of the two primary leaders is subsequently reactivated by restressing the gap are still obscure and, apart from the fact that the shorter leader is never reactivated if it ended in a restrike (see Section 4.1), the reactivation of one or other of the primary channels is very random.

Nevertheless, the presence of the space charge injected by the nonreactivated leader must be taken into account when modelling the reactivation of the basic leader. This is especially important when the basic leader is the shorter, because a large amount of positive space charge is left in the gap between the basic leader and the plane. To study the reactivation process further it will thus be necessary to simulate the development of the primary discharge.

From the present study we see that, in developing a suitable model, the most important parameter influencing the primary leader propagation would appear to be the relative inception time of the two leaders.

10.2 Charge structure of reactivated leader and leader-corona systems

A. ROBLEDO-MARTINEZ and R.T. WATERS

10.2.1 Aims of model: Records have been obtained during these experiments where the charge flow, leader spatial growth and electric field changes can be measured for both the basic leader and its subsequent reactivation. It was noted in Section 4 that charge flow and space-charge field data showed major differences in these two successive stages. The aim of this contribution is to employ a simplified structural model of the leader channel and its corona to account for these differences in terms of space charges.

10.2.2 Method of simulation:

(*a*) *Model structure:* The spatial form of the discharge is represented here by the simplified structure shown in Fig. 24. An axial line charge of linear density Q_z and length Z represents the leader channel. The leader corona from the channel tip is shown as a ring charge of radius R at a distance C ahead of the tip. The model postulates that a net charge density Q_z on the leader can be regarded as unipolar, but that a significant spatial separation of charge can occur in the leader corona. There will be an excess Q_s of positive charge, on the streamers of the leader corona, and the charge separation is represented by an axial dipole moment P_s of the ring. For the numerical simulations to be described here, the dipole moment P_s was constrained to be positive; in physical terms this would represent the normal direction of charge separation in the applied field.

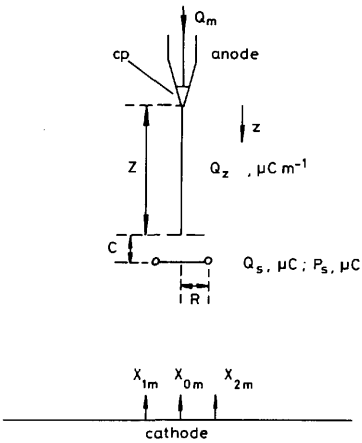

Fig. 24 *Discharge model*

cp = Current probe; Q_m = measured charge
Z, Q_z = length, charge density of axial channel, respectively
R, Q_s, P_s = radius, charge and dipole moment of axial ring, respectively
X_{im} = space-charge fields at plane

For economy of computation, the six parameters of this model were reduced to four (Z, Q_z, Q_s, P_s) by fixing $C = 0.75$ m and $R = 0.5$ m. These C, R values were reasonably representative of the leader-corona extent. The four remaining parameters were then varied iteratively, and for each combination of parameter values four externally measurable quantities Q_c, X_{0c}, X_{1c} and X_{2c} were computed. These were, respectively, the charge flow which would be measured at the current probe in the rod tip, and the corresponding space-charge field at three positions on the plane electrode. These computed values, together with the axial length Z at each iteration, were then compared with the actual measured values of the quantities Q_m, X_{0m}, X_{1m}, X_{2m} and Z_m. The best fit of the computed and measured values of these quantities then allowed the parameter values of the spatial quantities Q_z, Q_s and P_s to be compared for the basic and the reactivation stages. Although the actual values obtained for these parameters are of course dependent on the constraints of the simplified structural model which was chosen, they show significant differences between the two stages.

(*b*) *Coefficients for computation of charge and field values:*

(*i*) *Charge coefficients:* Fig. 25 shows the results of a charge-simulation computation of the per-unit potential $\bar{U}(z)$ along the gap axis for the condition that both of the main rod and plane electrodes are at zero potential, with the exception of the current probe at the rod tip, which is at unit potential. For this computation the presence of external boundaries was neglected. From the Shockley-Ramo theorem, the charge measured at the current probe for an axial element of length Δz at location z is then

$$\Delta Q = Q_z(1 - \bar{U}(z))\,\Delta z \tag{1}$$

The calculated charge flow for a leader of length z is thus

$$Q_{c1} = Q_z \int_0^z (1 - \bar{U}(z))\,dz = q_1 Q_z \tag{2}$$

Values of q_1 are shown in Table 7 as a function of channel length Z. A further component Q_{c2} of measured charge

Table 7: Charge coefficients

Z m	q_1 m	q_2 —	q_3 10^{-3} m^{-1}
0.5	0.44	0.991	7.2
0.75	0.69	0.993	4.88
1	0.93	0.994	3.89
1.25	1.17	0.995	2.91
1.5	1.43	0.996	2.42
1.75	1.68	0.996	1.93
2	1.93	0.997	1.77
2.25	2.18	0.997	1.40
2.5	2.43	0.997	1.25
2.75	2.68	0.998	1.10
3	2.93	0.998	1.01

flow will arise associated with Q_s. The calculation of Q_{c2} requires computation of the per unit potential $\bar{U}_1(r, z)$ at off-axis locations with a radial co-ordinate $r = 0.5$ m. Then

$$Q_{c2} = Q_s(1 - \bar{U}_1(r, z)) = q_2 Q_s \tag{3}$$

The dipole moment P_s also contributed an amount Q_{c3} to the calculated charge flow. The electrostatic principle involved here is that a dipole of moment p at a location with per-unit field $\bar{E} = d\bar{U}_1(r, z)/dz$ causes an associated charge flow pE. Thus

$$Q_{c3} = -P_s \, d\bar{U}_1(r, z)/dz = q_3 P_s \tag{4}$$

Calculations of q_2 and q_3 as a function of channel length Z are given in Table 7 for $C = 0.75$ m and $R = 0.5$ m. The total calculated charge flow for the parameter values of the model is then

$$Q_c = Q_{c1} + Q_{c2} + Q_{c3} \tag{5}$$

(ii) *Field coefficients:* The charge simulation also enabled the space-charge electric field at the plane to be calculated for a line charge of linear density Q_z. This field X_{c1}, is shown in per-unit form $e_{01} = X_{c1}/Q_z$ in Table 8 for the central position on the plane. Similarly the field due to the ring charge Q_s can be calculated. Fig. 26 shows these fields for three radial positions on the plane electrode for $Q_s = 1$ μC. Table 8 lists the per-unit field $e_{02} = X_{c2}/Q_s$ for the central probe, again as a function of leader channel length Z.

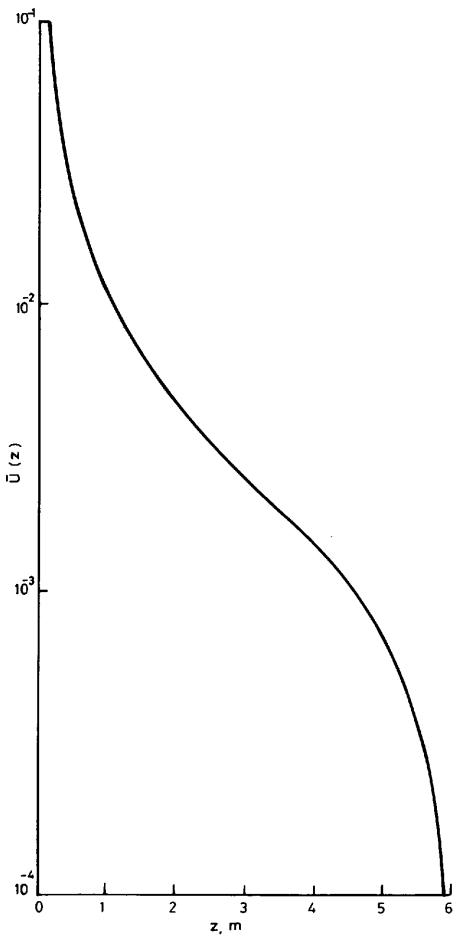

Fig. 25 *Per-unit potential for charge flow analysis*
$\bar{U}(z)$ = axial potential for $U(cp) = 1$ and U (anode, cathode) = 0

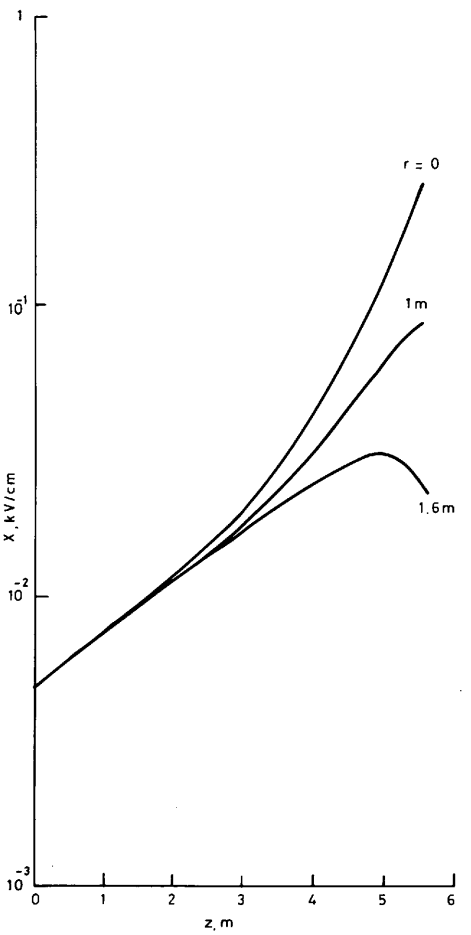

Fig. 26 *Field induced at plane electrode by ring charge*
$R = 0.5$ m; $Q_s = 1$ μC;
r = radial position on plane

The field X_{c3} created at the central probe by the dipole moment P_s is found from the derivative with respect to z of

Table 8: Field coefficients for central probe

Z m	e_{01} kV/μC	e_{02} 10^{-3} kV cm^{-1} μC^{-1}	e_{03} 10^{-5} kV cm^{-2} μC^{-1}
0.5	0.24	8.7	3.6
0.75	0.41	9.7	3.8
1	0.58	10.9	4.7
1.25	0.83	12.1	5.6
1.5	1.08	13.8	7.3
1.75	1.32	15.5	9.0
2	1.57	18.1	10.7
2.25	1.98	20.6	12.4
2.5	2.38	25.0	19.3
2.75	2.80	28.5	26.2
3	3.20	35.5	33.1

the per-unit field e_{02}. Then

$$X_{c3} = P_s\, de_{02}/dz = e_{03} P_s \tag{6}$$

Then the total calculated field at the central probe is given by superposition:

$$X_{0c} = X_{c1} + X_{c2} + X_{c3} \tag{7}$$

Similar coefficients to those tabulated in Table 7 have been obtained for the other probe positions, so that X_{1c} and X_{2c} can be calculated for the model parameters Z, Q_z, Q_s and P_s.

(*c*) *Test for fit:* The optimum choice for the model parameters Z, Q_z, Q_s and P_s for the basic and reactivated leaders of a given discharge was obtained by means of a minimisation of the expression

$$D = \left[0.2\left\{\left[\frac{Z - Z_m}{Z_m}\right]^2 + \left[\frac{Q_c - Q_m}{Q_m}\right]^2 + \left[\frac{X_{0c} - X_{0m}}{X_{0m}}\right]^2 + \left[\frac{X_{1c} - X_{1m}}{X_{1m}}\right]^2 + \left[\frac{X_{2c} - X_{2m}}{X_{2m}}\right]^2\right\}\right]^{1/2} \tag{8}$$

To calculate D (minimum), the interval on the leader channel length Z was first chosen. The appropriate set of twelve charge and field coefficients q_i and e_{ij} were then called up during the model parameter iterations. The calculation of the measurable charge and field values utilised the relationships:

$$\begin{bmatrix} Q_c \\ X_{0c} \\ X_{1c} \\ X_{2c} \end{bmatrix} = \begin{bmatrix} q_1 & q_2 & q_3 \\ e_{01} & e_{02} & e_{03} \\ e_{11} & e_{12} & e_{13} \\ e_{21} & e_{22} & e_{23} \end{bmatrix} \begin{bmatrix} Q_z \\ Q_s \\ P_s \end{bmatrix} \tag{9}$$

10.2.3 Results: Table 9 shows a typical selection of D (minimum) values from the test sequence using impulse combination 1 (see Table 2). With a few exceptions, these are typical of the quality of fit obtained between the model and the measured values of charge, field and leader length. It is noticeable from Table 9 that the quality of the mean fit to the measured values is better (about $\pm 3\%$ to $\pm 11\%$) for the basic discharge than those of the reactivated discharge ($\pm 8\%$ to $\pm 36\%$).

As an example of the parameter values obtained with a good fit to both discharge phases, Table 10 gives details for shot 6 of Table 9. The per-unit fit of Q_c/Q_m and the

Table 9: D(minimum) values

Shot number	1	2	3	4	5	6	7	8
Basic discharge	0.03	0.05	0.05	0.05	0.04	0.09	0.04	0.11
Reactivated discharge	0.18	0.09	0.28	0.36	0.20	0.08	0.11	0.16

electric field values are fairly uniformly good. The best-fit condition also gives good agreement (6–8%) between the

Table 10: Example of modelisation

Basic discharge			Reactivated discharge		
Measured values	Per-unit fit	Model parameters	Measured values	Per-unit fit	Model parameters
$Q_m = 87$	0.99	$Q_z = 0.5$	$Q_m = 28$	1.05	$Q_z = 0$
$X_{0m} = 0.77$	1.00	$Q_s = 40$	$X_{0m} = 0.56$	0.97	$Q_s = 30$
$X_{1m} = 0.88$	0.85	$P_s = 10$	$X_{1m} = 0.48$	1.09	$P_s = 32$
$X_{2m} = 0.67$	1.12	$Z = 1.0$	$X_{2m} = 0.58$	0.90	$Z = 1.25$
$Z'_{1b} = 0.94$	1.06		$Z_{2D} = 1.35$	0.92	

Combination 1(*b*) $U_+ = 240/9000$ μs, 1390 kV, $\Delta t = 800$ μs, $U_- = 40/165$ μs, 690 kV
Qs, *Qm*(μC); *Xm*(kV/cm); *Z*(*m*); *Qz*(μC/cm); *Ps*(μC m)

length Z of the model channel and the respective lengths Z'_{1b} and Z_{2D} at withstand of the basic and reactivated leaders. The value of $Q_z = 0.5$ μC/cm obtained for the charge per unit length on the basic leader channel is typical of the value usually estimated. In fact, the main contrast between the model parameters in Table 10, for the basic and reactivated discharges, lies in this leader charge density Q_z and also in the leader-corona dipole moment P_s. A zero charge density Q_z is estimated for the reactivation phase. On the other hand, a much greater dipole moment (32 μC m compared with 10 μC m) is estimated for the reactivation phase.

The results of Table 10 are typical of the general behaviour in these experiments. Fig. 27 shows the parameter values of Q_z, Q_s and P_s for the eight discharges of Table 9, where the numerical subscripts 1 and 2 denote the basic and reactivated discharges, respectively. It is seen from Fig. 27*a* that the model shows the leader charge density Q_{z2} to be negligible for all reactivated discharges. The net charge Q_{s2} on the reactivated leader corona is, according to the model, often about 50% of the net charge Q_{s1} for the basic discharge (Fig. 27*b*). The dipole moment P_{s2} for the reactivated discharge was usually larger than for the basic discharge.

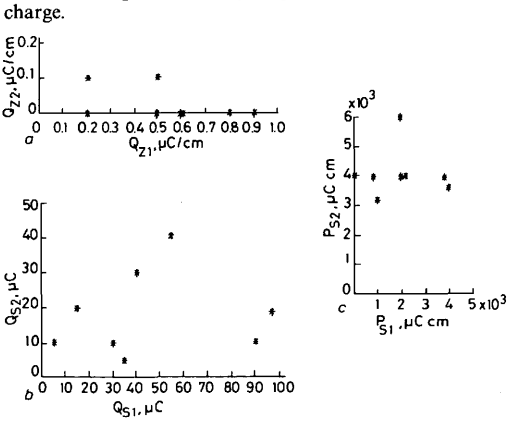

Fig. 27 *Model parameter values for basic and reactivated discharges*
Impulse combination 1

As in all numerical modelling, it is important to test the sensitivity of the fit of the measured data to changes in the parameter values. Again for the particular basic discharge of Table 10, Fig. 28 shows the variation of the test function D to individual variation in the parameters Q_z, Q_s and P_s, the remaining two being held constant. The sensitivity to changes in Q_z and Q_s appears to be good. The sensitivity to changes in P_s is lower.

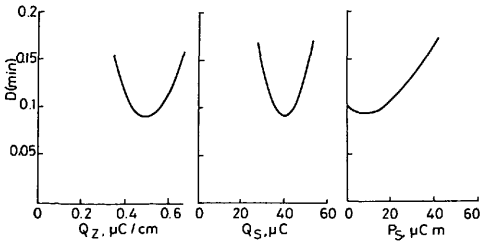

Fig. 28 *Sensitivity test of model parameters for discharge of Table 10*

10.2.4 Conclusions: The differences in the measured values of space-charge field X and charge flow Q for basic and reactivated discharges are shown by the model to be best accounted for by a significant charge separation and deposition in the leader corona of the reactivation process. Little further charge is deposited on the leader channel of the previously established leader.

10.3 Leader decay: Model based on drift, space-charge expansion and ion combination

M. DAVIES, J.E. JONES, and R.T. WATERS

10.3.1 Introduction: The test results presented in this paper have shown that the time characteristic of the decay of the leader channel conductivity is of the order of 1 ms. The main objectives of the work which is briefly described in this Appendix are to contrast the influence of two decay régimes which will be present, and to estimate the effect which these régimes will have during the observed times for leader reactivation and decay. The first régime causing leader deionisation is ion drift. The other régime employs the two processes of space-charge expansion and ion combination. As all three processes are dependent on the neutral gas density, some uncertainty concerning the conditions within the leader channel is inevitable. The relative air density k with respect to NTP within the channel is therefore used as a parameter for these calculations. The strioscopic studies of the tests have allowed some quantitative estimates to be made of appropriate k-values.

Two leader geometries have been used. The first considers the leader as a circular cylinder, with a constant potential gradient along its length. The second assumes a conical shape, which is a closer representation of true leader conditions: the strioscopic records show that the channel is tapered, so that the cross-sectional area diminishes with distance from the anode. For this latter geometry, the potential gradient is assumed to increase with distance from the electrode. This assumption can be justified from earlier leader-channel studies.

Results are presented and assessed in terms of the decay of the negative-ion density which has been plotted as a function of time and axial position in the leader channel.

10.3.2 Decay processes:

(*a*) *Drift:* The leader channel may be regarded as a nearly neutral cold plasma. The local value of k is such that the E/n value will be sufficient to maintain the electron population for current continuity. When leader growth ceases, a rapid fall in the electron population will be caused by the cessation of the leader corona, the electron loss to the anode and the attachment within the leader channel. The positive and negative small ions of densities n_+ and n_- will still be subject to the prevailing field, which is the resultant of space charge and applied fields. These fields are known not to change rapidly on leader arrest. Fig. 29 shows the two sweeping actions

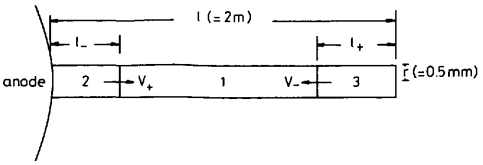

Fig. 29 *Representation of the cylindrical model of the leader channel showing the various regions*

Region 1 is the bipolar central section; regions 2 and 3 are the unipolar negative and positive regions, respectively.

which the field imposes on the ion populations. The central region 1 is contracting because of the drift of positive ions away from the anode in region 2, and the drift of negative ions towards the anode at the leader tip which is region 3. Deionisation by drift can be regarded as being complete when the central region vanishes, so that the channel has been effectively denuded of negative ions.

The velocities of the boundaries are the drift velocities of the ions, namely

$$V_+ = \frac{\mu_+}{k} E \quad \text{and} \quad V_- = \frac{\mu_-}{k} E \tag{10}$$

where the NTP values of the mobilities are taken as

$$\mu_+ = 1.4 \times 10^{-4}\ \text{m}^2/\text{Vs} \quad \text{and} \quad \mu_- = 1.8 \times 10^{-4}\ \text{m}^2/\text{Vs} \tag{11}$$

(*b*) *Space-charge expansion and combination:* In addition to the small-ion losses by drift, in the central region of the leader there will be losses from space-charge expansion and also the combination of small ions with others of opposite polarity or with neutral particles. The governing equations which are appropriate to cylindrical leader channels are similar to those which have been used to study corona decay [6]. These read as follows:

$$\frac{dn_-}{dt} = \frac{\mu_- n_- e}{k\varepsilon_0}(n_+ - n_-) - \alpha_r n_- n_+ - \eta_{21} n_- N_+ - \eta_{20} n_- N_0 \tag{12}$$

$$\frac{dn_+}{dt} = -\frac{\mu_+ n_+ e}{k\varepsilon_0}(n_+ - n_-) - \alpha_r n_- n_+ - \eta_{12} n_+ N_- - \eta_{10} n_+ N_0 \tag{13}$$

$$\frac{dN_-}{dt} = \eta_{20} n_- N_0 - \eta_{12} n_+ N_- \tag{14}$$

$$\frac{dN_+}{dt} = \eta_{10} n_+ N_0 - \eta_{21} n_- N_+ \tag{15}$$

$$\frac{dN_0}{dt} = \eta_{12} n_+ N_- + \eta_{21} n_- N_+ - \eta_{10} n_+ N_0 - \eta_{20} n_- N_0 \tag{16}$$

where N_-, N_+ and N_0 are the number densities of large negative and positive ions and of neutral particles, respectively. Also

α_r = small ion combination coefficient
η_{12}, η_{21} = coefficients of combinations between small and large ions
η_{10}, η_{20} = coefficients of combinations between small ions and neutral particles
e = electronic charge
ε_0 = permittivity of free space

The space-charge expansion process is described by the first terms on the right-hand sides of eqns. 12 and 13. Eqns. 12 to 16 have been numerically solved using forward differences, in which a useful check on the accuracy of calculation is that

$$N_- + N_+ + N_0 = \text{constant} \tag{17}$$

10.3.3 Leader models:

(*a*) *Cylindrical leader channel:*

(i) *Initial conditions:* It is first necessary to choose the value of the parameter k. A constant value is adopted for the whole channel (this implies a constant temperature throughout the channel). Strioscopic measurements imply that the most probable range of values of k are between 0.05 and 0.25. The k-value influences not only the mobilities (eqn. 10), but also the combination coefficients of eqns. 12 to 16. The following values were used for these coefficients [7]:

$$\left.\begin{aligned} \alpha_r &= 2 \times 10^{-12}\, k^{3/2}\ \mathrm{m^3/s} \\ \eta_{12} &= 5 \times 10^{-12}\, k^{3/2}\ \mathrm{m^3/s} \\ \eta_{21} &= 6 \times 10^{-12}\, k^{3/2}\ \mathrm{m^3/s} \\ \eta_{10} &= 3 \times 10^{-12}\, k^{3/2}\ \mathrm{m^3/s} \\ \eta_{20} &= 4 \times 10^{-12}\, k^{3/2}\ \mathrm{m^3/s} \end{aligned}\right\} \tag{18}$$

A preliminary analysis showed that the small-ion decay was insensitive to the initial values of N_+ and N_-; these were thus set to zero. The appropriate value of N_0 probably lies in the range $10^9\ k$ to $10^{12}\ k$; a sensitivity calculation again showed that the choice for N_0 was not critical, and a value of $N_0 = 10^{10.5}\ k$ was used. The time origin $t = 0$ was chosen to be at the instant of cessation of leader growth and current interruption. The initial value of $(n_-(t))_{t=0} = n_-(0)$ was chosen on the assumption that this corresponded to the free electron population n_e immediately before leader arrest. On this basis, continuity of current in the leader gives

$$I = n_e e \mu_e E \pi r^2 \tag{19}$$

where the following values are assumed:

electron mobility $\mu_e = 8 \times 10^{-2}\ k^{-1}\ \mathrm{m^2/Vs}$

leader gradient $E = 1\ \mathrm{kV/cm}$

channel radius $r = 0.5\ \mathrm{mm}$ (20)

and the leader current I is typically 0.5 A. Hence,

$$n_-(0) = 5 \times 10^{20} k^2/\mathrm{m^3} \tag{21}$$

Preliminary calculations also showed that, for $n_-(0) \neq n_+(0)$, equalisation of $n_-(t)$ and $n_+(t)$ in the central region occurred after a very short time. Thus, $n_-(0)$ and $n_+(0)$ were set equal in the main calculation. The overall leader length was taken to be 2 m, which approximates to the maximum value for nonbreakdown events in the present tests.

(ii) *Results:* Fig. 30 shows the per-unit variation with time of $n_-(t)/n_-(0)$ in the central region, for the relative density values of $k = 0.05$, $k = 0.1$ and $k = 0.25$. The deionisation rate due to combination and space-charge expansion is easily the greater for $k = 0.25$. On the other hand, the drift process is faster for $k = 0.05$, when the unipolar regions at $t = 1$ ms are of lengths $l_- = 0.36$ m and $l_+ = 0.28$ m.

In these unipolar regions, ion density decay has been shown to be dominated by space-charge expansion, and is very rapid.

(*b*) *Conical leader channel:*

(i) *Initial conditions:* The same combination coefficients, initial values, and values of leader current and length were used as for the cylindrical model. In this more sophisticated model, the base area of the cone was taken as 5 mm^2 and the potential gradient was assumed to vary linearly with the distance x from the anode as shown in Fig. 31. These assumptions with current continuity result in the initial negative-ion density $(n_-(x, t))_{t=0} = n(x, 0)$ being given by

$$n_-(x, 0) = \frac{k \times 10^{20}/m^3}{(1 - x/2)^2(0.5 + 2.25x)} \tag{22}$$

where x is measured in metres. This function, which is shown in Fig. 31, has a singularity at $x = l(=2\ \mathrm{m})$, but this does not affect the calculations in the central region 1.

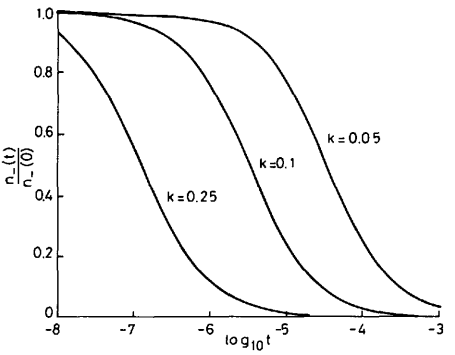

Fig. 30 *Decay profiles of the negative ion density in the cylindrical channel in region 1 for various values of the relative air density k*

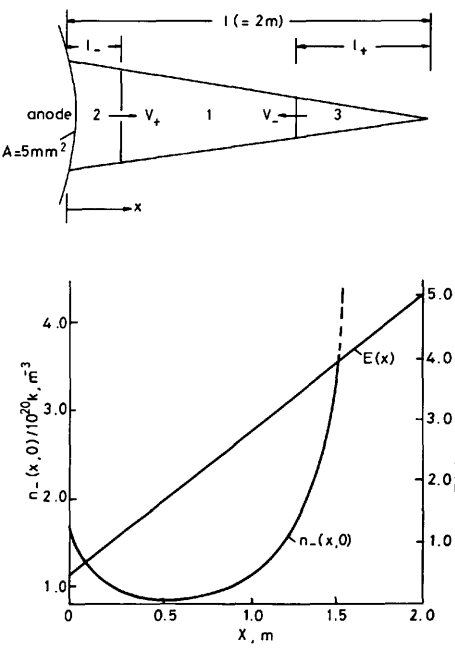

Fig. 31 *Representation of the conical model (regions 1, 2 and 3 as for Fig. 29), and plots of the initial negative ion density $n_-(x, 0)$ and field strength $E(x)$*

The curve of $n_-(x, 0)$ has a minimum at (0.52, 0.85).

A further complication is the constricting and dilating effects that the fixed geometry of the cone imposes on the positive and negative small ions, respectively, as they move in the leader channel. Continuity conditions similar to eqn. 19 can be used to show that the extra time rates of change in the ion number densities at a fixed point in the channel, because of these effects, are

$$-\frac{\mu_-}{k}\frac{dE}{dx}n_-(x, t) \quad \text{and} \quad \frac{\mu_-}{k}\frac{dE}{dx}n_+(x, t) \tag{23}$$

for the respective ions. Eqns. 12 and 13 now have to be modified for this geometry, to read

$$\frac{dn_-}{dt} = \frac{\mu_- n_- e}{k\varepsilon_0}(n_+ - n_-) - \frac{\mu_-}{k}\frac{dE}{dx}n_- - \alpha_r n_- n_+ - \eta_{21} n_- N_+ - \eta_{20} n_- N_0 \tag{24}$$

$$\frac{dn_+}{dt} = \frac{\mu_+ n_+ e}{k\varepsilon_0}(n_+ - n_-) + \frac{\mu_+}{k}\frac{dE}{dx}n_+ - \alpha_r n_- n_+ - \eta_{12} n_+ N_- - \eta_{10} n_- N_0 \tag{25}$$

where the extra terms have been shown to be numerically small when the parameters are as chosen here.

(ii) *Results:* Eqns. 24, 25, 14, 15 and 16 have been solved numerically and the results are shown in Fig. 32. The per-unit negative-ion density profiles $n_-(x, t)/n_-(x, 0)$ within the central region together with the boundaries of the central region have been drawn for increasing times. The limiting k-values are again 0.05 and 0.25. As before, the deionisation rate in the central region is far more rapid for $k = 0.25$, but the drift effect is significant for $k = 0.05$, particularly in the tip region. Regions 2 and 3 are again quickly deionised by space-charge expansion.

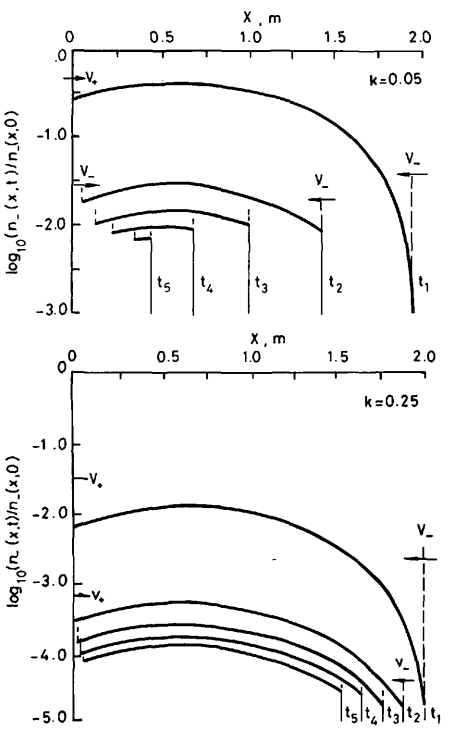

Fig. 32 *Plots of n_- in the conical channel as a function of x at increasing times for the two extreme values of k*

Times t_1, t_2, t_3, t_4 and t_5 are 1.5×10^{-5} s, 3.75×10^{-4} s, 7.5×10^{-4} s, 1.125×10^{-3} s and 1.5×10^{-3} s.
The contraction of the central region by the sweeping action of the field is also shown.

10.3.2 Conclusions: The calculations show that significant leader deionisation can be expected within a time of 1 ms. The three processes of drift, space-charge expansion and ionic combination may all be significant. Their relative importance is highly dependent on the relative density k within the channel. This behaviour of the model is consistent with the A and B phases observed in the leader reactivation process; more precise physical information is still needed.

10.4 Thermodynamic decay of the leader channel after the discharge arrest

I. Gallimberti and S. Stangherlin

10.4.1 Introduction: The results presented in this paper, part 2, have shown that, in the case of phase-to-phase insulation, when subsequent delayed overvoltage pulses are applied to the phase electrodes, a leader discharge can develop during the first pulse and survive in the inter-electrode space for times of the order of milliseconds. This leader discharge can then be reactivated during the second pulse, and, in some cases, can lead to breakdown of the gap.

However, the electrostatic and thermodynamic conditions within the leader discharge should decay in time, as it has been observed that the reactivation activity decreases when the delay Δt is increased, becoming inefficient after 2–3 ms.

The reactivation processes have been analysed in detail (Figs. 3–6): they consist of a fast first phase (phase A), during which a fraction of the basic leader channel is suddenly reilluminated (with no significant current and charge flow) and restored into a conductive state; then a second slower phase follows (phase B) during which the new leader and its front corona propagate within the old channel with a relatively high velocity (5–10 cm/μs) and low charge (~ 10 μc/m). After the old leader track has been completely covered, the new leader emerges into the free space (phase D) and propagates with the usual velocity (1–2 cm/μs) and charge (~ 50 μc/m).

These results indicate that part of the old basic leader is immediately available in an adequate conductive state to support the process of leader-streamer advancement; the remaining part has lost the conductive properties, but remains at higher temperature and lower gas density than the surrounding gas, leading to a preferential ionisation path.

The fraction of the leader channel which keeps adequate conductive conditions (z_{2A}/z_{1b} in Fig. 14) decreases with increasing Δt, from 1 at $\Delta t = 400$ μs, down to 0 for Δt larger than 1500 μs. In the mean time the leader channel is observed to expand slowly (Fig. 20), also in the absence of any energy input from the external circuit.

The aim of this paper is to present a discussion of the relevant decay processes of the leader discharge, and a model of the leader cooling phenomena, which appear to explain satisfactorily the experimental observations.

10.4.2 The leader discharge and the decay processes: Under the present experimental conditions, the leader discharge (Fig. 33) is composed by two clearly distinct dis-

charge regions [3, 4, 8]: the leader channel, which is a relatively high temperature, conducting plasma filament

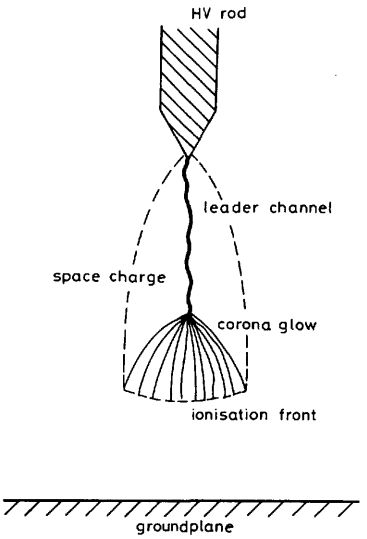

Fig. 33 *Schematic representation of the leader discharge in long airgaps*

(temperature 3000–6000 K, longitudinal field 1–5 kV/cm, current 0.1–10 A), and the corona glow which is a diffuse cold region of net positive space charge, composed mainly by positive and negative ions surrounding the leader channel. An ionisation front at the boundary of the glow region, supports the leader elongation by feeding current and energy into the leader head; in front of the head (Fig. 33) a transition in temperature and conductivity occurs between the cold diffuse glow and the hot filamentary leader channel: owing to its relatively high conductivity the leader tip acts as a current 'collector', leading to a concentration of current density, electric field and specific power input around the tip: it has been assumed [8] that the increase of temperature above a threshold value of about 1500 K can cause the detachment of the negative ions and hence increase conductivity, which corresponds to the leader formation.

The temperature distribution along the leader channel is not uniform, but it increases with the age of each leader section, from the head towards the HV rod: in fact the older sections have encountered a larger charge flow and energy input [9]; for the same reason the older sections have expanded to a larger radius than the younger ones.

When the activity of the leader discharge stops, the current drops to zero, and all processes of charge deposition and energy input are arrested. Dissipative phenomena then start the leader discharge decay, which consists of two main processes: (*a*) the neutralisation of the corona space charge and (*b*) the change of the thermodynamic conditions within the leader channel.

(*a*) *Space charge neutralisation:* The neutralisation of the space charge is essentially related to its movement. In fact local recombination of positive and negative ions does not affect the net space charge and the electric field distribution within the gap.

The ion movement is related to mobility, which, in turn, depends on the ion nature: the primary ions produced by ionisation, or attachment, are rapidly converted by charge exchange into secondary types which are then clustered within a few microseconds by a number of water molecules [10]. On a longer time scale, the ions can also remain attached to dust particles, forming massive ions of very low mobility [11].

Owing to all these conversion processes, it is not easy to study the movement of the space charge. However, the average ion mobility on a millisecond timescale can be assumed to be certainly lower than 1 $cm^2/V \cdot s$ [12]. This implies that, in the actual fields (1–10 kV/cm), the space charge cannot move more than a few centimetres per millisecond. This is consistent with fluxmeter measurements [3, 4].

It can be therefore concluded that space charge movement and neutralisation occur on a much longer timescale than that observed during the present experiment for the leader discharge decay. This is in agreement with the experimental observation (Fig. 3) that all the field measurements on both electrodes remain practically unchanged during the time delay Δt before the application of the negative voltage. Furthermore, there is experimental evidence of the insignificant change of the space charge on a millisecond time scale, in the fact that the reactivated leader deviates from the space charge clouds created by restrikes of the original leader (Fig. 17).

(*b*) *Leader thermodynamic conditions:* During the activity of the leader discharge the internal conditions within the leader channel are determined by the resistive energy flow, which can cause continuous (normal propagation) or sudden (restrike) gas temperature increase and channel cross-section expansion.

Spectroscopic results [13] indicated that during the leader discharge activity no local thermodynamic equilibrium is obtained within the leader channel. The electron temperature is much higher then the gas temperature, while the vibrational excitation tends to be relaxed with a delay of a few tens of microseconds. The electron density and the channel conductivity are both related to the current flow and remain much higher than the Saha's values for thermodynamic equilibrium [8].

In the present experiment, it has been shown that the channel expansion is directly related to the charge flow (Fig. 4, Part 3): this indicates that the leader channel expands with an almost constant mass [8, 9], the heated gas inside the channel acting as a piston on the surrounding cold gas.

When the current conduction stops, however, the cross-section/charge characteristics become vertical (Fig. 4, Part 3) and the channel is observed to continue its expansion, in the absence of charge flow, for about 1 ms (Fig. 20). This is probably due to the thermal diffusion of the hot leader channel. Heat is transferred to the surrounding gas through the channel walls by conduction, while particles of the surrounding gas move towards the channel core to balance the cooling pressure decrease. The leader decay no longer keeps constant the mass within the channel.

When the current goes to zero, the electron density and the channel conductivity tend to follow the current drop. They reach quite rapidly the thermodynamic equilibrium values of Saha's equation and, in addition, the vibrational excitation relaxes within about 10 μs [8]. The leader decay occurs, therefore, under local thermodynamic equilbrium conditions. Furthermore, the channel cooling occurs sufficiently slowly to assume that pressure equilibrium is realised everywhere. During the cooling process, the electron density and the conductivity in the channel will follow the temperature decay; maintaining the equilibrium values given by Saha's equation.

A first estimate of the order of magnitude of the thermal diffusion time constant indicate that the leader cooling should occur on a millisecond timescale, which would be consistent with the present experimental results.

10.4.3 Model of the leader thermodynamic decay: Let us consider a section of the leader channel. The aim of the simulation is to derive the neutral density and temperature distributions over the cross-section and their variations with time.

We assume local thermodynamic and pressure equilibrium. If air is assumed to be a nonviscous fluid, and the kinetic transport energy is neglected with respect to the internal energy, the energy conservation equation can be written in the form [14]:

$$\operatorname{div}(\lambda \overline{\operatorname{grad}}\, T) = \operatorname{div}(\rho h \bar{v}) + \frac{\partial}{\partial t}(\rho h) \tag{26}$$

where T represents the gas temperature, ρ the gas density, h the specific enthalpy per unit mass, $\bar{v}$ the transport velocity and λ the thermal conductivity.

Eqn. 26 states the first principle of thermodynamics for an isobaric transformation in a nonviscous fluid. The enthalpy change per unit time within the control volume equals the enthalpy flux due to mass transport and heat conduction across the walls of the control volume.

The mass conservation equation can be written in the form:

$$\frac{\partial \rho}{\partial t} + \operatorname{div}(\rho \bar{v}) = 0 \tag{27}$$

As there are no mass sources, the change of mass per unit time equals the mass flux through the walls of the control volume.

The gas state equations have to be added to eqns. 26 and 27. For isobaric transformations, the specific enthalpy change is related to the temperature change through the constant pressure specific heat C_p, i.e.

$$\partial h = C_p\, \partial T \tag{28}$$

and the gas density is related to the temperature by the ideal gas state equation

$$p = R\rho T \tag{29}$$

where p is the pressure and R the gas constant. In the present case R is temperature-dependent. It depends, in fact, on the average molecular mass of the gas particles, which is affected by the dissociation of O_2 and N_2 molecules and, inversely, by the recombination of the O and N atoms. Under isobaric conditions, eqn. 29 represents, therefore, a nonlinear state relationship between ρ and T (Fig. 34*a*).

Dissociation and recombination processes do not appear directly in the mass eqn. 27 because they do not affect the specific mass density ρ. On the contrary, dissociation and recombination appear indirectly in the energy eqn. 26, because they influence the specific heat C_p, and, hence, the specific enthalpy h.

If rotational symmetry is assumed for the leader channel, and the longitudinal variations of the thermodynamic quantities are neglected with respect to the radial ones, eqns. 26 and 27 can be written in the forms:

$$\frac{\partial}{\partial r}\left(\lambda \frac{\partial T}{\partial r}\right) + \frac{\lambda}{r}\frac{\partial T}{\partial r} = \rho v_r \frac{\partial h}{\partial r} + \rho \frac{\partial h}{\partial t} \tag{30}$$

$$\frac{\partial \rho}{\partial t} + \frac{\partial \rho v_r}{\partial r} + \frac{\rho v_r}{r} = 0 \tag{31}$$

To solve this system and obtain the time evolution of the temperature radial profile, the radial velocity v_r has to be

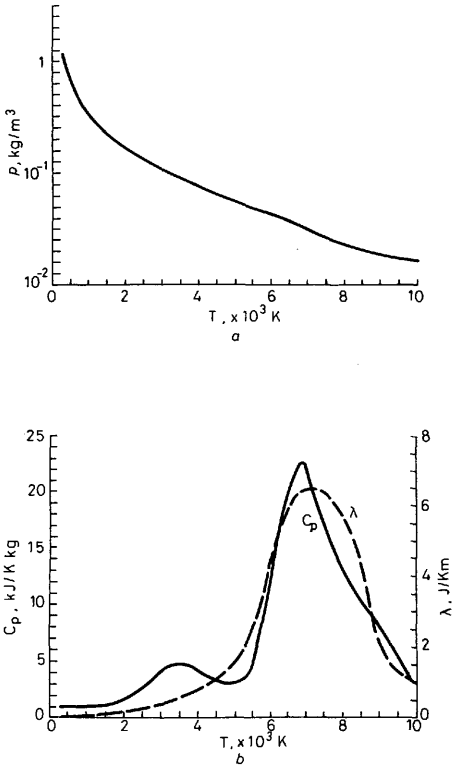

Fig. 34 *Thermodynamic characteristics of air at 1 bar as functions of the temperature*

a The density ρ; *b* The specific heat at constant pressure C_p and the thermal conductivity λ

eliminated from eqns. 30 and 31. Substituting eqn. 28 into eqn. 30, and integrating eqn. 31 over the leader cross-section, from the Gauss theorem we obtain

$$\rho C_p \frac{\partial T}{\partial t} = \lambda \frac{\partial^2 T}{\partial r^2} + \left(\frac{\lambda}{r} + \frac{\partial \lambda}{\partial r} - \rho v_r C_p\right)\frac{\partial T}{\partial r} \tag{32}$$

$$\rho v_r = \frac{1}{r}\frac{\partial}{\partial t}\int_0^r r\rho\, dr \tag{33}$$

Eqn. 33 gives the term ρv_r to be used in eqn. 32. This equation system is strongly nonlinear: the specific heat C_p and the thermal conductivity λ are both nonlinear functions of the temperature (Fig. 34*b*). C_p has two marked peaks around 4000 and 7000 K, corresponding to the dissociation of O_2 and N_2, respectively, while λ has a peak due to the contribution of chemical reactions to heat transfer.

The system of eqns. 32 and 33 can be solved numerically with a finite difference method.

10.4.4 Finite difference procedure: Let us consider a bidimensional integration grid. The index i marks the advancement in the r-direction by steps Δr (from $i = 0$, $r = 0$ to $i = i_{max}$, $r = r_{max} = i_{max} \cdot \Delta r$); the index j marks the advancement in time by steps Δt (from $j = 0$, $t = 0$ to $j = j_{max}$, $t = t_{max} = j_{max} \cdot \Delta t$).

The assigned boundary conditions are the following:

(*a*) $j = 0$, $t = 0$: A gaussian profile is assumed for the temperature

$$T(r) = T_0 + (T_{10} - T_0) \exp\left(-\frac{r^2}{a_0^2}\right) \tag{34}$$

where T_0 is the ambient temperature, T_{10} is the initial temperature on the leader axis and a_0 is the radial position at which the temperature drops to T_{10}/e. Such a gaussian temperature profile is roughly consistent with the radial density profiles derived for the leader channel from schlieren pictures.

The initial radial velocity distribution has been assumed to be simply related to gas diffusion

$$\rho v_r = -D\frac{\partial \rho}{\partial r} = -D\frac{\partial \rho}{\partial T}\cdot\frac{\partial T}{\partial r} \tag{35}$$

and has been, therefore, simply calculated from the initial temperature profile; however, the results of the numerical simulation have shown to be almost completely insensitive to the initial choice of ρv_r.

(*b*) $i = 0$, $r = 0$: Symmetry conditions impose $\partial T/\partial r = 0$ and $v_r = 0$ on the leader axis.

(*c*) $i = i_{max}$, $r = r_{max}$: To obtain significative results, the position r_{max} has to be chosen where the gas is unperturbed. Therefore, both conditions $T = T_0$ or $\partial T/\partial r = 0$ are adequate for the outer boundary.

We assume that all the thermodynamic quantities in eqns. 32 and 33 are known at a generic time interval j (in all the radial points $i = 0$ to i_{max}) and we calculate their values at the subsequent time interval $j + 1$. Eqn. 32 can be expressed in finite differences in the form:

$$T_i^{j+1} = T_i^j + \frac{1}{\rho(T_i^j)C_p(T_i^j)}\left[\lambda(T_i^j)\cdot\left(\frac{\partial^2 T}{\partial r^2}\right)_i^j + \left(\frac{\lambda(T_i^j)}{i\,\Delta r} + \frac{\lambda(T_{i+1}^j) - \lambda(T_{i-1}^j)}{2\,\Delta r} - (\rho v_r)_i^j C_p(T_i^j)\right)\left(\frac{\partial T}{\partial r}\right)_i^j\right] \tag{36}$$

In eqn. 36 the first and second radial derivatives of the temperature can be calculated, respectively, with conventional 5-point and 3-point finite-difference formulas.

Near to the axis or to the outer boundary, the index i may exceed its natural limits ($0 \leqslant i \leqslant i_{max}$). The corresponding temperature values can be assigned by symmetry for $i < 0$, and by extrapolation of the boundary conditions for $i > i_{max}$.

Eqn. 36 makes it possible to calculate the temperature radial profile at time $j + 1$, except for the point on the channel axis, where $i = 0$ appears in the denominator. In fact, in eqn. 32 the term $(\lambda/r)\,\partial T/\partial r$ becomes indeterminate in the origin. However, the symmetry conditions on the channel axis and the application of the Gauss theorem show that

$$\lambda\left.\frac{\partial^2 T}{\partial r^2}\right|_{r=0} = \frac{\lambda}{r}\left.\frac{\partial T}{\partial r}\right|_{r=0} \tag{37}$$

which makes it possible to eliminate the indeterminancy from eqns. 32 and 36 for $r = 0$.

Eqn. 33 is then used to calculate the value of ρv_r at time $j + 1$:

$$(\rho v_r)_i^{j+1} = \frac{\Delta r}{i\,\Delta t}\cdot\left[\sum_{k=0}^{i} k(\rho(T_i^{j+1}) - \rho(T_i^j))\right] \tag{38}$$

Eqn. 38 does not hold for $i = 0$, but the boundary conditions assign $v_r = 0$ on the leader axis.

The finite-difference integration method can therefore be applied starting from $t = 0$, $j = 0$, where both temperature and velocity profiles are assigned by the initial conditions. To ensure numerical stability the condition

$$\max(v_r)\cdot\Delta t \ll \Delta r \tag{39}$$

must be satisfied everywhere.

10.4.5 Computed results: To represent leader sections of different 'ages', different initial profiles of temperature have been selected. With reference to the parameters of eqn. 34, an 'old' leader section has been represented with $T_{10} = 5000$ K and $a_0 = 0.8$ mm. The temperature is consistent with spectroscopic observations [13], and the radius a_0 is deduced from the actual observations at the end of the leader conduction phase. It should be noted that a_0 does not represent the leader radius, but only the point where the temperature decreases to T_{10}/e (see subsequent discussion on schlieren photographic radius). A younger leader section has been represented with $T_{10} = 3000$ K, $a_0 = 0.6$ mm. The radius in this case has been estimated according to the expansion with constant mass during the leader conduction phase. The results of the simulation are reported in Figs. 35, 36 and 37.

In Fig. 35 it is possible to see the change of the temperature profiles with time. The thermal diffusion process leads to a decrease of the central temperature value T_1, while the temperature near the channel outer boundary is raised. The latter effect is more pronounced for old leader sections ($T_{10} = 5000$ K) than for young ones ($T_{10} = 3000$ K). The cooling process is very fast at the beginning (Fig. 37*a*), particularly for leader sections at high temperature. However, it slows down later, and the decay timescale becomes consistent with the experimental observations.

The leader density profile (Fig. 35) has sharp edges which move in the outward direction, as a consequence of gas heating around the channel by thermal diffusion. The central value of the gas density ρ_1 increases with time (Fig. 36*b*) in inverse proportion to the temperature.

To represent quantitatively the characteristics of the channel expansion during the decay process, the variation with time of the radial position of points with constant relative or absolute temperature has been derived. In Fig. 37*a* the radii where the temperature decreases, respectively, to 50%, 36% (1/*e*), 20% and 10% of the central value T_1 are reported as functions of time. It clearly shows that broadening of the relative temperature distribution during the decay process.

However, if the radii of constant absolute temperature are plotted as functions of time (Fig. 37*b*), it can be clearly observed that the high-temperature core of the leader channel contracts until it disappears, while the low-temperature boundary layers expand. The time at which the high-temperature core disappears depends on the initial central temperature T_{10}. In a young leader section ($T_{10} = 3000$ K) the core with $T > 2000$ K disappears within 120 μs, while that with $T < 1500$ K disappears within 300 μs. In an old leader section ($T_{10} = 5000$ K) they disappear, respectively within 600 and 1200 μs.

The curve at 500 K represents at the same time the expansion of the points where the density decreases to about 50% of the unperturbed value (Fig. 37). This curve represents, therefore, the expansion of the walls of the density depression. To compare this expansion directly with the experimental radii derived from the schlieren

measurements, the points where the density decreases to 84%, 66% and 50% of the standard ambient value have been calculated and reported in Fig. 38 for an initial central temperature T_{10} of 5000 K. Quite satisfactory

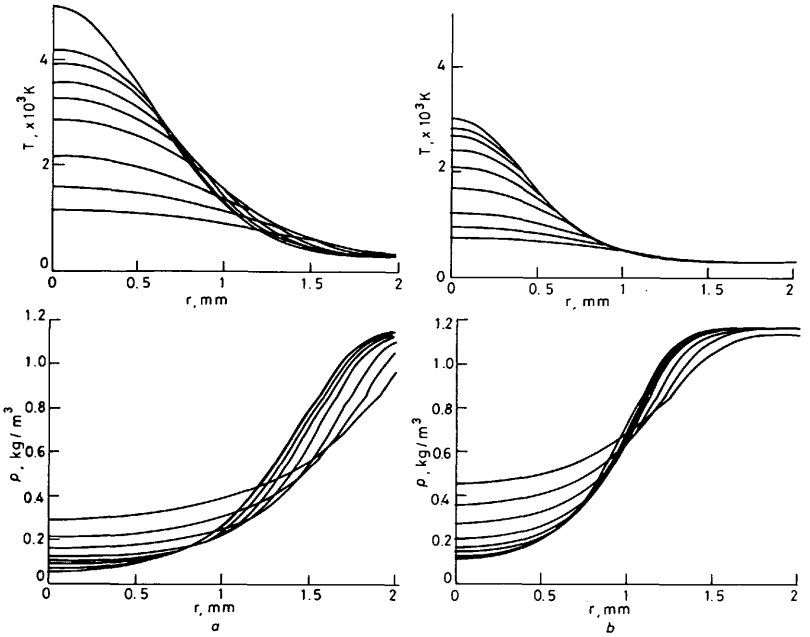

Fig. 35 *Temperature and density profiles during the leader thermal diffusion*

a 'Old' leader: $T_{10} = 5000$ K, $a_0 = 0.8$ mm; *b* 'Young' leader: $T_{10} = 3000$ K, $a_0 = 0.6$ mm

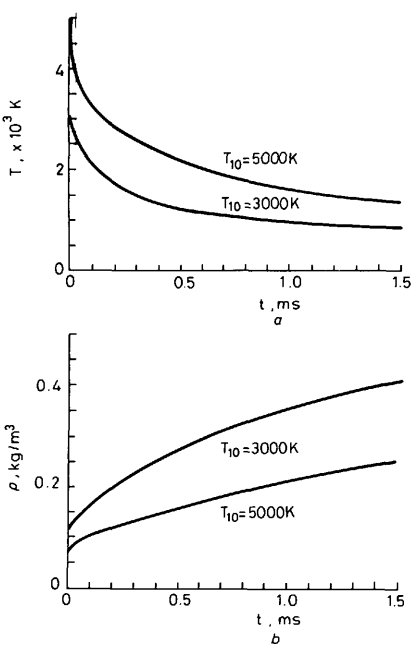

Fig. 36 *Variation with time of the temperature and density central values*

a Temperature T_1; *b* Density ρ_1

agreement between computed and experimental results is observed. The computed results indicate that with increasing time the channel walls become less sharp, which is consistent with the loss of definition that is experimentally observed in the schlieren photographs.

The rate of temperature decay is clearly changing with time (Fig. 36*a*) and depends on a number of parameters. To study this dependence, eqn. 32 has been particularised for $r = 0$. Taking into account eqn. 37, we obtain

$$\rho C_p \frac{\partial T_1}{\partial t} = 2\lambda \frac{\partial^2 T_1}{\partial r^2} \tag{40}$$

If a gaussian approximation of the type in eqn. 34, with radius a, is used for the temperature profiles for $t > 0$, we obtain

$$\frac{1}{T_1 - T_0} \frac{\partial T_1}{\partial t} = -\frac{4\lambda}{\rho C_p a^2} \tag{41}$$

This equation gives the decay of the central temperature value. The instantaneous time constant

$$\tau = \frac{\rho C_p a^2}{4\lambda} \tag{42}$$

depends on the instantaneous values of the temperature T_1 and of the radius a (Fig. 39). It varies from a few tens of microseconds at the highest temperatures down to a few milliseconds at the ambient temperature. The time constant τ is proportional to the mass within the channel ρa^2 and to the ratio between specific heat and thermal conductivity, which represents the specific cooling rate.

From eqn. 41 it is possible to calculate the times at which the high-temperature core disappears. We have

$$\frac{\partial t}{a^2} = -\frac{\rho C_p}{4\lambda(T_1 - T_0)} \partial T_1 \tag{43}$$

and, because the first member in this equation is a function of time only, while the second member is a function of the temperature T_1 only, it is therefore possible to integrate to give

$$t_c = \bar{a}^2 \int_{T_c}^{T_{10}} \frac{\rho C_p}{4\lambda(T_1 - T_0)} dT_1 = \int_{T_c}^{T_{10}} \frac{\tau}{T_1 - T_0} dT_1 \quad (44)$$

Here t_c represents the time at which the central temperature falls below T_c (starting from T_{10}), and $\bar{a}$ represents an average value of the channel radius during the cooling process (see curves 36% in Fig. 37). As already stated, the time t_c depends on the initial and final temperatures T_{10} and T_c and is proportional to the channel cross-section.

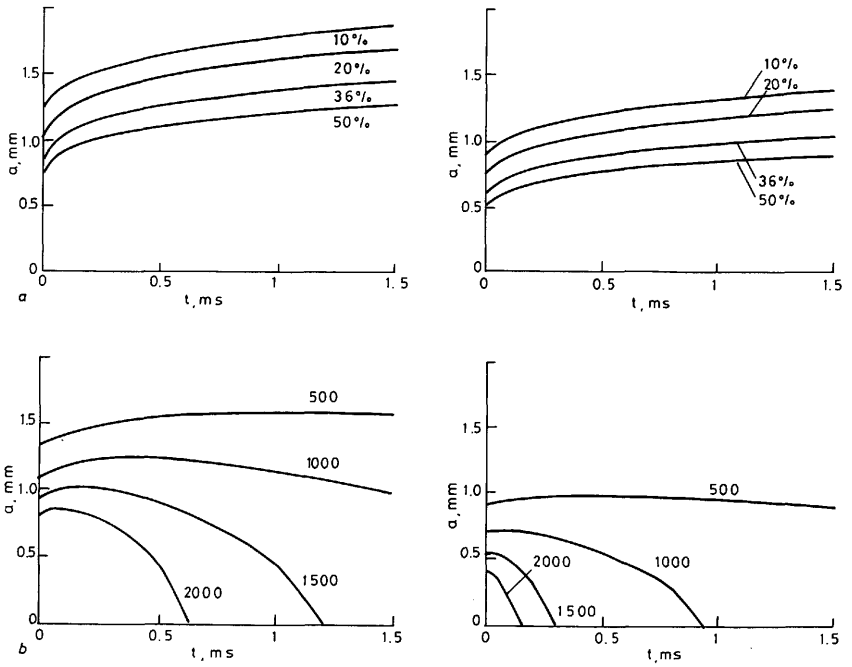

Fig. 37 *Variation with time of the radial position of points with constant relative or absolute temperature*

a radii, where T is a given percentage of T_1; *b* Radii, where T has a given value

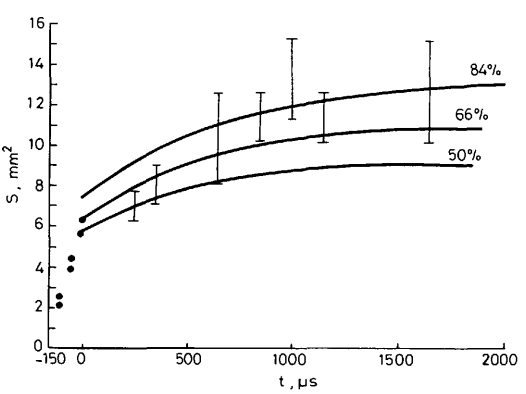

Fig. 38 *Comparison between the experimental measurements of the leader schlieren radius, and the computed radii where the density is, respectively, 84%, 66% and 50% of that of ambient air*

The negative fraction of the timescale represents the leader conduction phase.

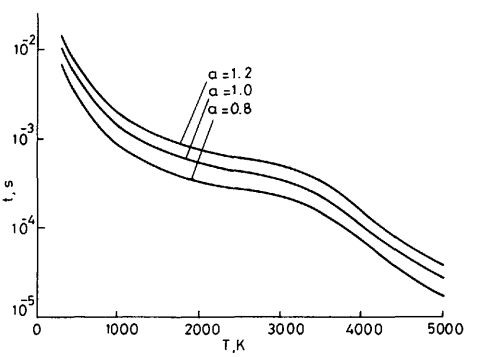

Fig. 39 *The time constant of central temperature decay as a function of the temperature itself, for different values of the radius a*

The temperature distribution along the leader channel at the beginning of the decay process has been calculated with the model described in Reference 8 and is reported in Fig. 40, together with the critical time t_c, computed for $T_c = 1500$ K and $\bar{a} = 1.2$ mm (which corresponds to an average schlieren section in Fig. 38 of about 9–10 mm^2).

The value $T_c = 1500$ K has been selected because it represents the leader formation temperature [8]. Above 1500 K, detachment is predominant with respect to attachment, and the negative ions produce free electrons, giving rise to a relatively high conductivity. The opposite is true below 1500 K. It can be therefore assumed that a leader channel section loses its conducting properties at time t_c when the temperature falls below 1500 K.

This makes it possible to calculate from Fig. 40 the fraction L_{2A}/L_1 of the leader channel which can maintain con-

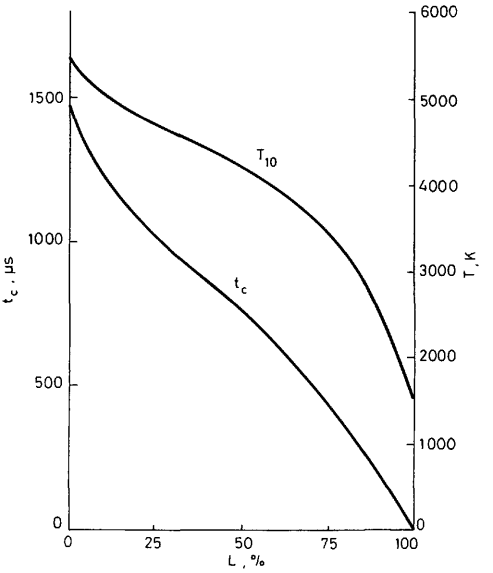

Fig. 40 *Computed distributions of the central temperature T_1 and of the critical time t_c along the leader channel*

ducting properties after a time interval Δt during the decay process, and to compare it with the experimental observations (Fig. 41). The average experimental curve (dashed line) is in excellent agreement with the computed results (solid line). The experimental points present, however, a large statistical scatter, due to the random fluctuations of the discharge characteristics and to the fact that the conductivity change with the temperature does not present a sharp transition around 1500 K.

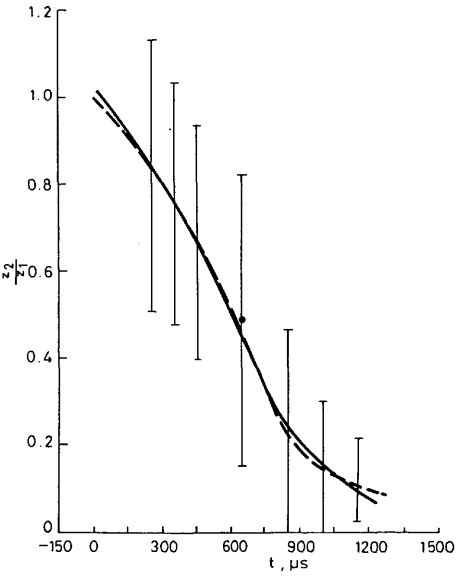

Fig. 41 *Comparison between the experimental and calculated values of the fraction of the leader length which maintains conductive properties after a time interval Δt*

The negative fraction of the timescale represents the leader conduction phase.

10.4.6 Conclusions: The presented discussion and the results of the simulation indicate that the leader decay is mainly associated with cooling by thermal diffusion. The calculated characteristics of this process are in good agreement with the experimental observations.

If it is assumed that the leader channel maintains its conductive characteristics only at temperatures higher than 1500 K, the fraction of leader length which is immediately reactivated (phase A), at the application of a delayed overvoltage, can be predicted with a very good approximation.